2018

Development of Forward and Inversion Schemes for Cross-Borehole Ground Penetrating Radar

Donald Jones
University of North Florida, n00624173@ospreys.unf.edu

Development of Forward and Inversion Schemes for Cross-Borehole Ground Penetrating Radar

by

Donald Craig Jones, P.E.

A thesis submitted to the School of Engineering

in partial fulfillment of the requirements for the degree of

Master of Science in Civil Engineering

UNIVERSITY OF NORTH FLORIDA

College of Computation, Engineering, and Construction

October, 2018

The thesis "Development of Forward and Inversion Schemes for Cross-Borehole Ground Penetrating Radar" by Donald Craig Jones, PE in partial fulfillment of the requirements for the degree of Master of Science in Civil Engineering has been approved by the thesis committee:

Nick Hudyma, PhD PE Thesis Advisor and Committee Chairperson	Date
William Dally, PhD PE Committee Member	Date
Christopher J. Brown, PhD PE Committee Member	Date
O. Patrick Kreidl, PhD Committee Member	Date

Accepted for the School of Engineering

Osama Jadaan, PhD Director, School of Engineering	Date

Accepted for the College of Computing, Engineering, and Construction

William Klostermeyer, PhD Interim Dean, College of Computing, Engineering, and Construction	Date

Accepted for the University of North Florida

John Kantner, PhD, RPA Dean, Graduate School	Date

DEDICATION

To my wife Erin for her support and constant encouragement, which have allowed me to pursue my many passions and vast interest, and to our children Juliette, Beatrice, and Evangeline, who can distill all the wonder of the world into a single expression and give the joy of eternity in little more than silence. Most of this was authored with at least one in my lap and with all of them in my thoughts.

ACKNOWLEDGMENTS

I would like to thank Dr. Hudyma for my introduction into GPR tomography and for maintaining persistent motivation and guidance throughout the research and writing of this thesis. I would also like to thank the committee members: Dr. Christopher Brown, Dr. Bill Daly, and Dr. Patrick Kreidl for their involvement and willingness to take on this thesis.

TABLE OF CONTENTS

TABLE OF TABLES

TABLE OF FIGURES

ABSTRACT

Tomography is an imaging technique to develop a representation of the internal features of material using a penetrating wave, such as an electromagnetic wave. The calculation method used is an example of an inverse problem, which is a system where the input and the output are known but the internal parameters are not. These parameters can be estimated by understanding the responses of penetrating wave as it passes through the unknown media. A forward problem is just the opposite; the internal structure and input penetrating wave is known and the output is determined. For both forward and inverse problems, raytracing is needed to define the raypath through the medium and inversion techniques are using to minimize the error for a discretized matrix of material properties. To assess various inversion techniques for use in shallow karst conditions, three synthetic karst geology models, each with increasing complexity, were generated. Each model was analyzed using forward modeling techniques to compare the calculated tomograms from known geometry and material properties. Gaussian Raytracing with LSQR inversion technique performed the best. This technique, Gaussian Raytracing with LSQR, was then applied to an inversion problem; cross-borehole ground penetrating radar data was collected at a karst geology field site and tomograms were produced. The resulting tomography confirmed information detailed in the driller's logs and features between boreholes were identified. This confirmed that cross-borehole ground penetrating radar is an applicable technique for use in geotechnical site characterization activities in karst areas.

Chapter 1

INTRODUCTION

Tomography is an imaging technique to develop a representation of the internal features of material using a penetrating wave, such as an electromagnetic wave. The calculation method used is an example of an inverse problem, which is a system where the input and the output are known but the internal parameters are not. These parameters can be estimated by understanding the responses of penetrating wave as it passes through the unknown media. In ground penetrating radar (GPR) tomography, an electromagnetic wave in the radar frequency range is transmitted from an antenna. The wave penetrates the media and propagates. The GPR wave responds to the electromagnetic properties of the material and reacts in a predictable manner. A receiving antenna located some distance away from the transmitting antenna collects the signal. This information is then used to develop a mathematical formulation that describes the material.

1.1 Applications of Cross-borehole GPR Tomography

Most of the State of Florida is underlain by thick carbonate deposits. These deposits form several geological units, such as Ocala Limestone and the Avon Park Formation, that comprise the Floridan Aquifer. The productivity of the aquifer is due to the development of secondary porosity from dissolution and other karst processes. Near-surface karst features play a dominant role in the hydrogeological and geotechnical framework of the state, especially in the Central and West regions. Due to karst processes, limestone formations are often heterogenous structures with variable depths and material properties. Urban developments, large infrastructure, and important assets are supported by these weathered limestone units. Subsidence events, such as sinkholes, can result in catastrophic structural damage. In

addition, the aquifer is one of the most productive in the world, providing water to 10 million people (Marella and Berndt, 2005) and karst features can create fracture zones able to transport surface-contaminants into the public drinking water supply (Stewart, 1982; Jones et al., 1994).

The ability of GPR tomography to determine moisture content and porosity of geological formations has led to many applications in hydrogeology and water resources engineering, such as refining aquifer models with high-resolution permeability estimates that can distinguish between matrix and fracture flow zones (Hyndman and Tronicke, 2005; Gloaguen et al., 2007); understanding vadose zone moisture dynamics and hysteresis of soil water-retention parameters (Cassiani and Binley, 2005); defining paleo, modern, and developing sinkhole geometries (Truss et al., 2007; Corin et al., 1997); solute transport in porous media (Day-Lewis et al., 2003; Tsoflias, 2004); non-aqueous phase liquid transport, containment, and treatment (Longino and Kueper, 1999); and monitoring gas emissions from soils (Comas et al., 2005). Due to the high-resolution of GPR tomograms, it has also found applications in geotechnical engineering and geology, such as stratigraphic characterization (Knight et al, 1997); mineral exploration and ore delineation (Bellefleur et al., 2000); determination of geotechnical properties (Kong, 1995); and site characterization (Lytle, 1978).

1.2 Comparison to Other Methods

Any penetrating wave can be used for tomography, such as magnetic resonance (fMRI), gamma radiation (SPECT), positron emission (PET), x-ray (CT), electrical capacitance (ECT), light absorption (ODT), and so on. In geological sciences and geoengineering, the most common methods are GPR, seismic, and electrical resistivity. In seismic tomography, a sound wave, called a seismic wave, is passed through a material and recorded some distance away. The wave produces small elastic deformations of the material. The product of these deformations is transmitted as two types of body waves: P-waves and S-waves (Liu and Gu, 2012). P-waves, or primary waves, produce a compressive deformation of the material along the axis of propagation. The velocity of the wave is a function of the density and shear modulus of

the material. S-waves, or secondary waves, produce a shear deformation of the material perpendicular to the axis of propagation. S-waves have a slower seismic velocity than P-waves, thus the two create distinct signals. Since, seismic waves directly measure the small-scale stress and strain parameters of a material, which can be correlated to the field-scale strength and stiffness properties of a material, it's often used for the geotechnical design of structures and public infrastructure (Keto and Kelamis, 2009). Seismic waves are expected to attenuate, or lose signal strength, at a much slower rate than radar waves. Therefore, it can be used in applications with large transmitter and receiver spacings.

A second common cross-borehole technique is electrical resistivity, or simply resistivity, tomography. Resistivity tomography applies an alternating current from a pair of electrodes while measuring current between the two probes using an ammeter. A separate pair of electrodes, or several pairs of electrodes, are placed some distance away. Using a voltmeter, voltage potential between the electrodes is measured. From Ohm's Law, resistivity is a function of the current density and the electric field. By transmitting a current into the material and measuring voltage within the material, the resistance across the material can be found (Loke, 2004). In general, there is a significant range for resistive properties of natural materials. This method can be used to distinguish the placement and classification of geological materials based on resistive valves (Herman, 2001).

1.3 Objectives

This thesis focuses on sub-surface imaging using ground penetrating radar (GPR) tomography. The main objective is to study the electromagnetic and geological phenomena in detail through modeling of a known dataset using numerical methods to simulate the propagation of electromagnetic waves. In particular, the model would allow the decomposition of different material parameters and describe the geological setting in which those properties may exist. These techniques are then applied to field data to formulate a tomogram using an unknown dataset. Field analysis and data collection was performed in a UNF-UF-FDOT test site in Alachua County Florida.

1.4 Thesis Layout

Chapter 2 provides a brief overview of Maxwell's Equations, which are the basis of GPR, and a description of the electromagnetic properties of geological materials. This is further developed to describe the electromagnetic wave equation and to create an ideal form of the GPR wavelet. Chapter 3 details the two common families of methods used to describe the propagation of an electromagnetic wave and the assumptions that are needed to reduce the problem into computational form. The first method assumes that the wave can be simplified to a quasi-linear path using Fermat's principle of least time. The second method recreates the wave by propagating a wavefront, an envelope that characterizes some property of the wave movement, such as the location of the leading edge at a particular time, through the media. Chapter 4 describes the common inversion techniques needed to resolve the boundary conditions into a matrix of material properties. The chapter begins with the simplest method used in practice and concludes with the most efficient method that's commonly used by commercial software packages (LSQR). Chapter 5 combines the techniques described in the previous chapters to develop a computer-based tomographic model of known and pre-defined material profiles. Three different material profiles are used; each one represents an increase in complexity. A model of the material properties (described in Chapter 2) is developed for each cross-section, then a GPR wave is modeled using the wave techniques from Chapter 3, and finally the system is solved using the inversion techniques described in Chapter 4. Chapter 6 will further develop these concepts using field data. Included in this chapter is a discussion of the expected and observed geological conditions, the field data collection techniques used, the data processing steps, and an interpretation of the results.

Chapter 2

GROUND PENTRATING RADAR MODELING

Cross-borehole tomographic measurements can be created by passing an electromagnetic (EM) pulse through a geological formation between two boreholes. A dipole antenna is lowered into the borehole to a known depth and triggered to emit a high-frequency electromagnetic pulse. The EM pulse propagates in the unknown medium and is recorded by a receiving antenna in the adjacent borehole a known distance away at a known depth. The receiving antenna records a wavelet of the voltage time-series, called a trace. The trace is analyzed to determine the travel time through the media. This information can then be used to identify the radar velocity of the unknown material between the boreholes, which can be correlated to material properties.

2.1 Electromagnetic Basis of GPR

2.1.1 GPR Antenna Properties

In its most basic form, a ground penetrating radar (GPR) system is simply a radar signal and a data recorder. The two are kept in sync with a common timer; the signals are transmitted and received through a pair of antennas. The circuitry is fundamental. The complexity of the system is largely attributed to the antenna. Unlike most antenna in production, GPR systems are not concerned with the information carried by the signal. For example, a communications antenna is designed to detect electromagnetic fields and translate, say, the modulation of radio frequency into information. In general, these antennas are as large as possible because the designers are interested in capturing as much of the signal as possible. The location of the signal is not important, just the temporal variation of

the signal. However, in GPR applications the designer is concerned with the onset of a signal at a particular spatial location. Source and detection points must be precise. This can be difficult to accomplish because the efficiency of EM generation and the reliability of EM collection is a function of antenna size and signal frequency. High-resolution GPR uses smaller antenna at the cost of efficiency and thus provides much less depth of penetration as opposed to, say, FM radio. This phenomenon can be observed during the selection of the first arrival travel times from the trace. To improve spatial accuracy, the antenna used for GPR applications have very short electric dipoles. The signal radiates uniformly in the plane perpendicular to the dipole with very little energy radiating from the ends of the dipole; forming a "donut" shaped EM amplitude at far-field distances (Annan 2009).

2.1.2 Wavelet Modeling

The signal radiating from the GPR antenna, known as a wavelet, is a complex function unique to the antenna construction and circuitry components. However, for impulse-style ultra-wideband systems, like GPR, a simple mathematical model (Eqn. 2-1) can be used for numerical simulation to model wave amplitude (s) over time (t) for a given radar frequency (f_c).

$$s(t,q,T) = v(t) - (2-q)v\left(t - \frac{T}{2}\right) + (1-q)v(t-T) \qquad \textit{Eqn. 2 - 1}$$

Where,

$$T = \left(\frac{2}{3} + \frac{1-q}{7}\right) \cdot \frac{1}{f_c}$$

$$v(t) = \frac{1}{2} \cdot \left(1 + \cos\left(\pi \cdot \frac{t - \frac{T}{2}}{\frac{T}{2}}\right)\right)$$

The dampening factor, q, aggregates the variability from the antenna design parameters into a single value. The factor is a real number between 0 and 1 (Figure 2-1). At its minimum value the wavelet forms a sinusoidal function of one cycle with a crest and trough of the same amplitude. At its maximum value the wavelet forms a sinusoidal function of one and one-half cycles with a greater initial crest amplitude than any following peak (Annan, 2009).

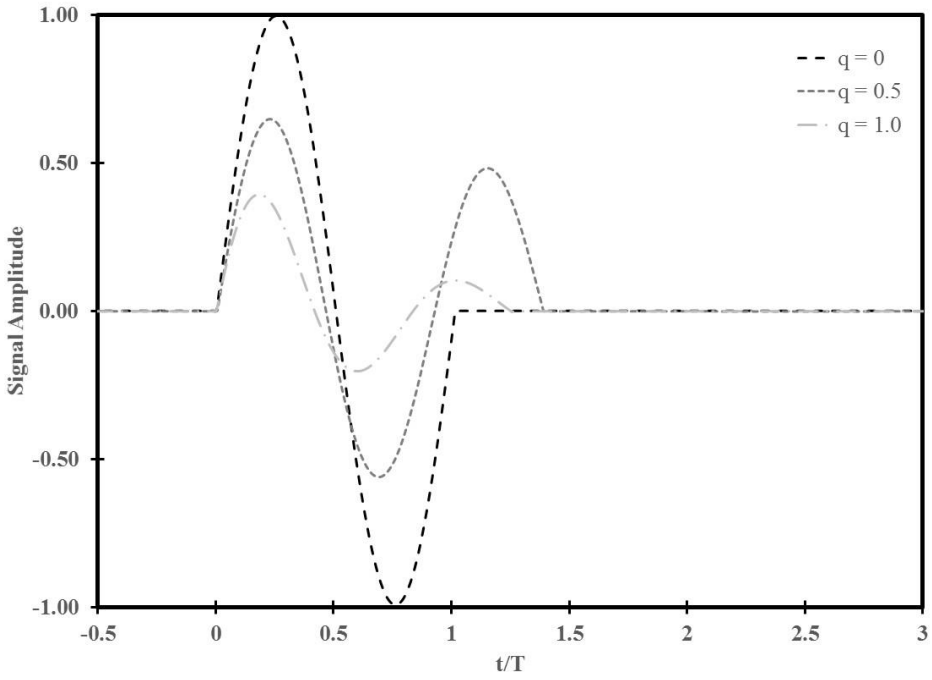

Figure 2-1, variation of the signal amplitude across several different damping parameters.

2.1.3 Electromagnetic Response

The GPR signal is a form of EM wave and thus can be derived from Maxwell's Equations. The received GPR response varies depending on the medium's electromagnetic (EM) properties, which are quantified using constitutive relationships to summarize the material properties. Maxwell's equations describe a time-varying coupled set of electric and magnetic fields. They are commonly represented as shown in Eqn. 2-2, Eqn. 2-3, Eqn. 2-4, and Eqn. 2-5.

Faraday's Law	$\nabla \times E = -\frac{\partial B}{\partial t}$	*Eqn. 2 - 2*
Ampere's Law	$\nabla \times H = J + \frac{\partial D}{\partial t}$	*Eqn. 2 - 3*
Gauss' Law	$\nabla \circ D = q$	*Eqn. 2 - 4*
Gauss' Law of Magnetism	$\nabla \circ B = 0$	*Eqn. 2 - 5*

Where,

E = Electric Field Strength
B = Magnetic Flux Density
D = Electric Displacement
H = Magnetic Field Intensity
q = Electric Charge Density
J = Electric Current Density

(Griffiths, 1999)

The physical properties of a material can be described on a macroscopic-level by aggregating the average behavior of the individual electrons, ions, and molecules. These generalizations form the parameters of the constitutive relationships: electrical conductivity (σ) (Eqn. 2-6), permittivity (ε) (Eqn. 2-7), and magnetic permeability (μ) (Eqn. 2-8). Electrical conductivity is a measure of how easily current can pass through a given material. Conductivity is the inverse of electrical resistivity. Most geological materials have a low conductivity in the absence of salinity, with the exception of some clay-rich soils. Permittivity is the ability to store and release an electrical energy. It is a function of electric field displacement and electric field strength. A higher permittivity means a lower electric flux. Lastly, magnetic permeability describes how the atomic moments respond to a magnetic field (Cassidy, 2009).

$$J = \sigma E \qquad \textit{Eqn. 2 - 6}$$

$$D = \varepsilon E \qquad \textit{Eqn. 2 - 7}$$

$$B = \mu H \qquad \textit{Eqn. 2 - 8}$$

2.1.4 The Electromagnetic Wave Equation

To better understand the relationship between the electric and magnetic fields, engineers assume an electric field is constrained to the y-axis that moves along the x-axis as a function of time. The curl of the simplified electric field (Eqn. 2-9) along with Faraday's Law (Eqn. 2-10) implies that the spatial variation of the electric field induces a time-varying magnetic field. Thus changing electric fields create magnetic fields that in turn induce electric fields and so on.

$$\nabla \times E(x,t)\hat{\jmath} = \begin{vmatrix} \hat{\imath} & \hat{\jmath} & \hat{k} \\ \partial/\partial x & \partial/\partial y & \partial/\partial z \\ 0 & E(x,t) & 0 \end{vmatrix} = \frac{\partial E}{\partial x}\hat{k} \qquad \textit{Eqn. 2 - 9}$$

$$\nabla \times E = -\frac{\partial B}{\partial t} \qquad \textit{Eqn. 2 - 10}$$

These alternating waves move perpendicular to each other in a direction that is orthogonal to both waves; thus the field moves coplanar with light waves. Depending on the magnitude of losses, the electromagnetic fields may propagate as waves. Mathematically, this is modeled using the transverse wave equation (Eqn. 2-11). This equation describes oscillations perpendicular to the direction of energy transfer. Mathematically, it is similar to S-Waves, or shear waves, observed in seismic applications (Annan, 2009).

$$\nabla \times \nabla \times E = -\mu\sigma \frac{\partial E}{\partial t} - \mu\varepsilon \frac{\partial^2 E}{\partial t^2} \qquad \textit{Eqn. 2 - 11}$$

The transverse wave equation is derived by first noting the closed character of the magnetic field, which can be expressed in terms of the electric field by applying the curl of Faraday's Law (Eqn. 2-12) to the modified form of Ampere's Law (Eqn. 2-13) and substituting the constitutive definitions (Eqns. 2-6 and 2.7).

$$\nabla \times \nabla \times E = -\frac{\partial}{\partial t}(\nabla \times \mu H) \qquad \textit{Eqn. 2 - 12}$$

$$\nabla \times \nabla \times E = -\mu \frac{\partial}{\partial t}(J + \frac{\partial D}{\partial t}) \qquad \textit{Eqn. 2 - 13}$$

2.1.5 Low-Loss Condition

The transverse wave equation (Eqn. 2-13) relies on the spatial and temporal second derivatives of the electric field. The system behaves as a wave where no (or little) energy is lost as it propagates through the medium. The first derivative of the electric field is the energy dissipation mechanism. The low-loss condition can be represented as the absolute relative magnitude of the first and second order terms, such that the low-loss criteria is satisfied where Eqn. 2-14 and Eqn. 2-15 are satisfied.

$$\frac{\mu\sigma\ \partial E/\partial t}{\nabla \times \nabla \times E} \ll \frac{\mu\varepsilon\ \partial^2 E/\partial t^2}{\nabla \times \nabla \times E} \qquad \textit{Eqn. 2 - 14}$$

$$\frac{\sigma\ \partial E/\partial t}{\varepsilon} \ll 1 \qquad \textit{Eqn. 2 - 15}$$

For sinusoidal time-varying fields, Eqn. 2-16 the above can be rewritten in terms of the angular frequencies (ω).

$$\frac{\sigma}{\varepsilon\ \omega} \ll 1 \qquad \textit{Eqn. 2 - 16}$$

Where,

$$\omega = 2\pi f \qquad \textit{Eqn. 2 - 17}$$

2.2 Material Properties

The propagation of an EM wave through the medium is a function of the EM properties that define the constitutive relationships. In most geological material, electrical properties are the dominant parameters in describing GPR behavior. In the absence of metallic materials, such as iron, magnetic variations are generally weak. The excitation of a material within an electric field creates movement of electric charges that induces a current flow; the magnitude of which is dependent on the material's properties. The electrical charges can be characterized as two general types: unbound and bound charges. These are respectively related to two types of current flow: conduction and displacement (Daniels, 2007).

Unbound, or free, charges give rise to conduction currents. For example, an electrical current moving through a copper wire is conduction current. Electrons move through the metallic matrix of the wire transferring charge from one point to another. The movement of ions in a water solution follows a similar mechanism. When an electric field is applied, the free charges quickly accelerate to a terminal (steady-state) velocity and then collide with neighboring atoms, electrons, or ions as it moves through the material. In a sense, the medium works against the movement of charges by these collisions.

Energy from the electromagnetic field is irreversibly transferred to mechanical energy in the form of heat (Cassidy, 2009). This is described in equation form as Eqn. 2-18.

$$J_C = \sigma E \qquad \textit{Eqn. 2 - 18}$$

Alternatively, bound charges are constrained to a limited distance of movement and are associated with displacement currents. When an electric field is applied, bound charges move to another static configuration. The electron cloud around an atomic nucleus is an example of this behavior, or the electrical charge in a small metal object embedded in an insulating environment (e.g. a capacitor). During the transition, energy is pulled from the electric field and stored in the material. When the field is removed, the charge moves back to its original configuration and energy is released. This is described in Eqn. 2-19. Permittivity is the constitutive property of a material to store and release electromagnetic energy in the form of an electric charge. Even in a vacuum, electric permittivity is non-zero. For GPR applications, permittivity is often provided as a non-dimensional relative permittivity, also referred to as the dielectric constant (k) in the literature (Daniels, 2007). The relative permittivity (ε_r) is the non-dimensional ratio of the material's true permittivity over the permittivity of a vacuum (8.85E-12 farads/meter).

$$J_D = \varepsilon \frac{\partial E}{\partial t} \qquad \textit{Eqn. 2 - 19}$$

The total electric current density (Eqn. 2-20) consists of the sum of Eqns. 2-18 and 2-19, one depends on the electrical field itself and the other on its rate of change. It is often stated in constitutive form (Eqn. 2-21).

$$J = J_C + J_D \qquad \textit{Eqn. 2 - 20}$$

$$J = \sigma E + \varepsilon \frac{\partial E}{\partial t} \qquad \textit{Eqn. 2 - 21}$$

Further, in sinusoidal time-varying fields, it is common to work in terms of angular frequency, such the total current density takes the form of Eqn. 2-22.

$$J = (\sigma + i\omega\varepsilon)E \qquad \textit{Eqn. 2 - 22}$$

In this formulation, the displacement current is 90° out of phase with the conduction current. The phase shift between the two currents describes the constructive and destructive nature of the electric field. One term (J_C) is an energy dissipation mechanism, and the other (J_D) is an energy storage mechanism. In a simple material, as described above, where the parameters are constant, there is a transition frequency where the conduction and displacement currents are equal. Below this frequency, the energy dissipating conductive currents dominate; above the energy storing displacement currents dominate. This frequency defines the onset of the low-loss regime important to the wave propagation of GPR and is often represented as the tangent of the angle between the two currents (Annan, 2007), known as the loss tangent (Eqn. 2-27).

Magnetic permeability describes how a charge alters the atomic spin of a material to create a magnetic dipole moment. In most GPR applications there is little magnetic influence on the propagation of electromagnetic waves (Olhoeft, 1998). For sedimentary rocks, the magnetic effects are assumed to be the permeability of free space (1.26E-6 henry/meter) with a relative magnetic permeability of one (Olhoeft, 1998).

Characterization using ground penetrating radar is most useful in low-loss materials, such as limestone and sand. Electromagnetic fields diffuse and propagate as waves when the amount of energy loss is small in comparison to the amount of energy stored. Within the geological environment high-loss materials, such as clayey soils and saline groundwater, prohibit penetration of GPR signals due to high conductivity values (Annan, 2009).

Water has a high relative permittivity, an order of magnitude higher than dry limestone. Therefore the saturation of the material has a pronounced effect on the radar velocity. For example, dry sand has an expected relative permittivity of 4.5 whereas a wet sand has an expected relative permittivity of 20. Because of the presence of water, there is significant overlap between material types. Radar velocity is not a unique indicator of material properties. However, the material properties can be disaggregated using several techniques.

2.3 Time-Propagation Mixing Model

Dielectric properties are primarily a function of minerology, porosity, water saturation, and other electrochemical interactions. Permittivity is a critical parameter in GPR tomography as it controls the velocity estimation, and thus the reflection coefficients for raytracing. Published values for permittivity of various geology can be found in the literature (for example Annan, 2009; Cassidy, 2009; Daniels, 2007). While broadly accepted, these values generalize complex mixtures of material, bedding types, and weatherization histories that can significantly vary between rock lithology. Several methods attempt to refine the estimate for permittivity based on other parameters. The two common approaches to the problem are empirical/semi-empirical estimates and volumetric models. Empirical/Semi-empirical estimates are derived from observed data without a specific physical model. Topp et al (1980) proposed the following estimate of total water content ($\theta_v = V_{water}/V_{total}$) based on the bulk relative permittivity of the medium (Eqn. 2-23).

$$\theta_V = -5.3 \times 10^{-2} + 2.9 \times 10^{-2}\mathcal{E}_b - 5.5 \times 10^{-4}\mathcal{E}_b^2 + 4.3 \times 10^{-6}\mathcal{E}_b^3 \qquad \textit{Eqn. 2 - 23}$$

Conversely, Roth et al (1990) found that the volumetric model can derive a relationship for the bulk permittivity (ε_b), or the permittivity of a composite material consisting of a unique mixture of possibly several materials, from the volume fraction of each of the soil or rock components using porosity (η) and total water content (θ_V):

$$\varepsilon_b = [\theta_V \varepsilon_{water}^{\beta} + (1-\eta)\varepsilon_{solid}^{\beta} + (\eta - \theta_V)\varepsilon_{air}^{\beta}]^{1/\beta} \quad \textit{Eqn. 2 - 24}$$

Testing has shown that beta (β) of 0.5 adequately represents isotropic two-phase mixed media (Roth et al., 1990). Therefore, the equation can be rearranged to the following equation, known as the time-propagation (TP) mixing model as a function of saturation (S) and porosity.

$$\varepsilon_b = [(1-\eta)\sqrt{\varepsilon_{solid}} + \eta S\sqrt{\varepsilon_{water}} + \eta(1-S)\sqrt{\varepsilon_{air}}]^2 \quad \textit{Eqn. 2 - 25}$$

2.4 EM Wave Attenuation

As the GPR wave propagates through the media, the strength of the signal degrades, or attenuates. Attenuation is the result of three phenomena: absorption, dispersion, and spherical divergence. Absorption is decay in amplitude caused by the energy loss due to heat conversion. When an electric field is applied, free charges accelerate and collide with nearby particles as a function of conductivity. These collisions cause thermal energy loss (Liu et al., 1998). Next, dispersion is the pulse deformation due to the frequency-dependence of the EM wave. Frequency-dependence is a function of the dielectric permittivity and mimics the attenuation behavior of seismic signals (Liu et al., 1998). Finally, spherical divergence is caused by the geometric spreading of the wave. Attenuation can be modeled as a reduction in amplitude, which can generally be described as a complex function of distance and time (Neto et al., 2006).

Assuming the dielectric properties are frequency independent in the GPR range (approximately 10-1000 MHz), a common assumption, attenuation can be described in terms of energy stored and energy released during the wavelet cycle. The effect is measured in terms of the Quality Factor, Q, which is shown as Eqn. 2-26 (Lui et al., 1998).

$$Q = \frac{\omega}{2c\alpha} \qquad \textit{Eqn. 2 - 26}$$

Where the attenuation coefficient is defined in terms of the loss tangent (Eqn. 2-27).

$$\alpha = \omega\sqrt{\frac{\mu\varepsilon}{2}}\sqrt{(1 + tan^2\delta)^{1/2} - 1} \qquad \textit{Eqn. 2 - 27}$$

The wave amplitude (A) is expected to decay exponentially as a function of the quality factor in low-loss media and wave frequency (f) over time (t), as described in Eqn. 2-28.

$$A(f,t) \propto \exp(\frac{-\pi f t}{\alpha}) \qquad \textit{Eqn. 2 - 28}$$

In non-magnetic, low-loss materials, where conductive attenuation is not the primary mode of amplitude reduction, the loss of signal strength is determined by dispersion of the EM waves. At the interface of different material properties, such as different saturations or lithology, a portion of the signal reflects off the boundary. The signal that continues to the receiving antenna is usually measured in terms of a dimension-less Power Reflectivity parameter, which is a function of the permittivity along the raypath. If the Power Reflectivity has less energy than background noise, the signal can be degraded beyond its useful signal-to-noise ratio (Annan, 1996). The received trace would be indiscernible. However, Yilmaz and Doherty (1987) found that by adding several traces from the same receiver and transmitter location the signal-to-noise ratio can be improved to usable levels. The technique is known as stacking. The Power Reflectivity is expected to increase by the square root of the number of stacks. In most GPR applications, several dozen stacks can be performed in rapid succession without noticeable delay in data collection.

2.5 Chapter Summary

This thesis studies the creation of tomograms by passing electromagnetic waves from a GPR antenna through geological media and recording the response. The focus of this chapter is to provide an understanding of the basis for GPR and its derivation from the fundamental Maxwell's equations. This discussion includes the physical phenomena of electromagnetic waves, their propagation and

attenuation. These properties are needed to describe the electromagnetic wave equation and to model GPR wavelets that will pass through the media. The electromagnetic properties of the geological materials are analyzed in terms of practical models that disaggregate the unique bulk material into its components, such as air, water, sand, clay, and limestone. These components can be used to calculate geotechnical properties such as porosity and saturation, which may be useful to hydrogeologists and geotechnical engineers.

Chapter 3

RAYTRACING SCHEMES

Distinct materials have unique electromagnetic properties, which can be simplified to radar velocity. When different materials occur adjacent to one another electromagnetic waves propagate by reflecting or refracting across the interface, similar to the reflection and refraction of light. The cumulative effect of these alterations creates a unique path through the media. When applied to the material's radar velocity, the travel time needed to traverse the media can be calculated from the path length for each cell. This is the first major component of tomography. By measuring the travel time between two points, a transmitter and a receiver, the path can be back-calculated using raytracing techniques. From the length of the path and the travel time, radar velocity is determined.

Two general families of raytracing techniques used: Raypath and Wavefront. Raypath techniques simplify the electromagnetic waves into quasi-linear paths through the media. There are two types of raypath raytracing methods described in this thesis: Geometric Raytracing and Gaussian Raytracing. Geometric Raytracing calculates the raypath based on the distinct values of the affected cells only, while Gaussian (Should this be Raytracing) Waveray takes a weighted average of the cells perpendicular to the raypath. Alternatively, wavefront techniques recreate the wave by propagating a wavefront through the media. In general, the wavefront is an envelope describing the leading edge of the electromagnetic wave at specified time intervals. Two methods of wavefront raytracing are discussed: NORSAR wavefront construction and Fast Marching Methods. Both are approximations of the Eikonal equations. NORSAR wavefront tracing is developed from Huygens' principle that each point is a source of secondary waves. The secondary waves are expanded from points along the previous wavefront and a new wavefront is

defined. The Fast Marching Method calculates travel time for each cell in an iterative procedure, starting at the transmitter location and expanding outward cell-by-cell until the entire cross-section has been analyzed. In addition, a final method is considered that combines elements of both families. Huygens' wavefront expansion determines the wavefront using raypath parameters.

3.1 Geometric Raytracing Method

3.1.1 Straight Raypath

In a discretized subsurface model, the raypath length through each cell can be defined by using any of several raytracing techniques. The simplest to implement, and least realistic, is the straight raypath method. This method assumes a linear path from the transmitter to the receiver, such that the initial ray angle is equal to the final ray angle, and any arbitrary angle in between (Cerveny, 2001).

There are two common algorithms to calculate the raypath length. The first is to define an arbitrarily small step along the horizontal axis. With the assumption that the material properties are homogenous within each cell, the ray angle will remain unchanged. The standard equation of a line can be used to find the positional change along the vertical axis. Pythagorean's theorem can be used to find the incremental raypath length and the new value accumulates with the previous values for that cell.

The second method is much more efficient and accurate, yet is requires more work for implementation. The premise is to identify which cell boundaries the ray will cross first, and then which cell the ray will move to. For example, starting from a transmitter depth of 8 meters and a receiver depth of 2 meters across a borehole separation of 10 meters, line equation has a slope of -0.6, or a raypath angle, θ, of $\mathrm{atan}(-0.6)$. The simple line equation for the raypath is $y = -0.6x + 8$. The next step is to determine if the ray is within the current cell at the leading horizontal boundary of the adjacent cell. In other words, does the ray cross the vertical edge first or the horizontal edge. Therefore, in the example provided, a first horizontal step along the x-axis corresponds to a vertical position of 7.4 meters (Eqn. 3.1)

$$y_1 = -0.6(1) + 8 = 7.4 \text{ meters} \qquad \textit{Eqn. 3 - 1}$$

If the transmitter location is defined as the center of the cell, the top of the cell should be 7.5 meters below ground surface at a 1 meter cell resolution. In this example, at the right edge of the cell, the ray will be outside of the current cell. The next step is to compute the exact location the ray crosses the cell's top edge (Eqn. 3-2).

$$x_1 = \frac{7.5-8.0}{-0.6} = 0.83 \text{ meters} \qquad \textit{Eqn. 3 - 2}$$

From Eqn. 3-2, the ray crosses the cell boundary at (0.83,7.5). The raypath length in the cell can be found using the distance formula as shown Eqn. 3-3.

$$d = \sqrt{(7.5 - 8.0)^2 + (0 - 0.83)^2} = 0.97 \text{ meters} \qquad \textit{Eqn. 3 - 3}$$

3.1.2 Curved Raypath Assumption

While simple to compute, in heterogeneous formations the straight raypath assumption is often not representative. Huygen's Principle states that quasi-spherical waveforms refract at the interface of two different materials. The formulation can be represented along this interface by a point source radiating secondary waves (Veselov, 2002). The sum of these secondary waves defines the refracted wavefront across the interface (Figure 3-1).

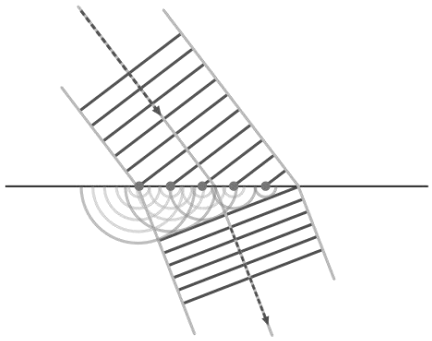

Figure 3-1: Refraction of a waveform across an interface using Huygen's Principle of secondary waves (after Nordmann, 2007).

This idea can be simplified from wavefronts to rays using Fermat's principle of least time. By incorporating this principle, diffuse waves are simplified to quasi-linear paths representing the shortest distance between two points orthogonal to Huygen's wavefronts. This allows an additional simplification. Instead of determining the wavefronts for each primary and secondary source, Snell's Law is used to track Fermat's raypath through the cross-section (Wolf, 1995).

3.1.3 Snell's Law

Snell's law describes the relationship between the raypath approach trajectory and the raypath exit trajectory after crossing the boundary between two isotropic material layers or discretized cells. Raypath vectors are parameterized in terms of the angle between the raypath and the plane normal to the interface at the point where the ray would cross the boundary, known as the angles of incidence. Snell's law relates the ratio of the sines of the approach and exit angles of incidence to the ratio of radar velocity found in the traversed media (Kauffmann and Glassner, 2002).

3.1.4 Critical Angle

There exists a critical approach angle where the existing ray is parallel to the boundary between the materials, or perpendicular to the normal plane, such that beyond this angle the raypath will reflect from the interface. Conceptually, this resembles a mirror image reflection of the ray across the normal plane.

The straight raypath assumption can be expanded by Snell's Law to create a raypath that varies across the different material boundaries, creating a curved raypath. In general for a ray travelling into material of higher velocity, the ray is "pulled" closer to the normal plane, while a ray travelling to a medium of lower velocity is "pushed" away from the normal plane. When this technique is applied to the entire cross-section a series of rays orthogonal to the wave propagation can be realized. However, the improved model adds new unknowns to the problem. For a given transmission location, varying initial radar path angles can have a non-linear effect on the terminal location of the ray. This can be problematic

since the tomographic model relies on accurate and consistent transmitter and receiver locations and angles.

The theoretical basis for raytracing using the curved path assumption was originally described by Wesson (1971) and Chander (1975), following research by Keller (1968) and Roberts and Shipman (1972). The two most common methods of geometric raytracing are the shooting method and the bending method. The shooting method, attributed to Dines and Lytle (1977), was originally documented by Engdahl (1973) to calculate earthquake locations in the Aleutian Islands. The intent is to find the starting angle that yields the intended receiver location. This is accomplished through an initial guess that is iterated using a method such as Newton-Raphson or the Secant method to minimize the error between the terminal end of the model raypath and the receiver location. The alternative method is the bending method, where the ends remain fixed and the ray is perturbed by an arbitrary parameter until the true ray is found (Julian and Gibbins, 1979). Cerveny (1987) applied these methods to GPR tomography. Of the two methods, the shooting method is far more common in practical cross-borehole applications.

3.2 Gaussian Waveray Tracing

The discretization of a potentially continuous natural formation may result in instances where the ratio change in the model assumptions for material velocity can significantly differ from the in-situ formation. This can cause sharp refractions or reflections in the tomogram that are not present in the field. A solution can be realized by smoothing the radar velocity along the raypath.

Gaussian waveray tracing relies on Huygen's principle to develop narrow-band wavefronts from secondary point-sources at the interface between discretized cells. The narrow band wavefront is defined as a contour of constant travel time. As the wavefronts propagate through the media a wavepath is formed (as opposed to a raypath). For simplicity, Lomax (1994) approximated the narrow-band wavefront at any time as a plane perpendicular to the wavepath. The velocity for each point on the wavepath is found by averaging the velocity along the instantaneous wavefront using a Gaussian weighting curve.

Following Eqn. 3-4, the wavefront average velocity ($\bar{v}$) at any point ($\vec{x}_v$) for an arbitrary travel time (T) can be described as the ratio of the integral of the weighted velocity in terms of the distance from the point over the integral of the Gaussian Weights, following derivation by Urdaneta (1994).

$$\bar{v}(\vec{x}_v, T) = \frac{\int \omega(\gamma) c[\bar{x}(\gamma, T)]\, d\gamma}{\int \omega(\gamma)\, d\gamma} \qquad \textit{Eqn. 3 - 4}$$

Where:

γ, is the distance from the point $\vec{x}_v$

$c[\bar{x}(\gamma, T)]$, is the velocity at distance γ from the point $\vec{x}_v$ for the T isochromatic contour

$\omega(\gamma)$, is the Gaussian Weight Curve for each distance γ from the point $\vec{x}_v$

In discrete form, the integral can be replaced by a finite sum over 2N+1 control points (Eqn. 3-5).

$$\bar{v}(\vec{x}_v, T) = \frac{\sum_{n=-N}^{N} \omega_n c[\vec{x}_v(T)]}{\sum_{n=-N}^{N} \omega_n} \qquad \textit{Eqn. 3 - 5}$$

The Gaussian Weight Curve, ω_n, is calculated from Eqn. 3-6.

$$\omega_n = \exp[-4\ln(2) \cdot ({}^{\gamma_n}/_{\alpha})^2] \qquad \textit{Eqn. 3 - 6}$$

The distance along the front, measured in wavelengths, is defined from Eqn. 3-7.

$$\gamma_n = \frac{n \cdot \gamma_{max}}{N} \qquad \textit{Eqn. 3 - 7}$$

Where N is the wave period (T) over the time step (Δt). Based on research by Lomax (1994) the curve-fitting parameters are often set to α = 2 and γ_{max} = 1.5. Given more information about the model, these parameters can be modified to reflect observed field conditions.

Smoothing the regularized velocity grid using Waveray Tracing increases the numerical stability of the tomographic inversion, compared to methods that have the potential for critical refractions from small changes such as curved-path geometric raytracing (Audebert et al., 2001).

3.3 NORSAR Wavefront Construction

Instead of calculating ray parameters from independently traced rays, as found in curved-ray geometric and Gaussian raytracing, it is possible to define the propagation of a GPR wave without raytracing. The method was first proposed by Vinje (1993) while working with the Norwegian Seismic Array (NORSAR). In instances where a uniform medium overlays a higher velocity medium, as often found in karst formations, this method is expected to give more reliable results than conventional raytracing (Tweeton, 2008). This method, known as NORSAR Wavefront Construction, relies on Huygen's principle to propagate wavefronts. The theory states that every point on a wave is a source of secondary waves and that the sum of those secondary waves determines the wavefront; where wavefront is defined as an isochrone traveltime contour that represents the wave location at a specific time.

To initialize, a circle is drawn about the point source with a radius defined as a function of the material's radar velocity. Then a series of points is drawn along the circular wavefront at regular intervals. From each of these points a circle, representing the secondary waves, is drawn proportional to the local material velocity parameter of the cell.

The sum of the secondary wavelets is then approximated by constructing lines tangent to adjacent isochrone circles. A smooth curve is then generated from the bisection of the two intersection points from the adjacent circles on each side of the current wavefront location. The process is repeated for all points until the wavefront is fully formed. Then a series of new points at regular intervals is drawn along the new wavefront and the process is repeated. The loop continues until the entire cross-section has been traversed (Urdaneta, 1994).

The wavefront is developed from the tangent lines between adjacent secondary waves and then smoothed by calculating the intersection point. The vector between the center of the adjacent circles can be defined in terms of length, d, and orientation angle, β, as measured from the vertical. Using Eqn.

3-8, the Pythagorean distance between adjacent center points is calculated. The orientation angle is determined using Eqn. 3-9.

$$d = \sqrt{(x_k - x_{k\pm1})^2 + (z_k - z_{k\pm1})^2} \qquad \textit{Eqn. 3 - 8}$$

$$\beta = \text{atan}(\frac{x_k - x_{k\pm1}}{z_k - z_{k\pm1}}) \qquad \textit{Eqn. 3 - 9}$$

Assuming a tangent line can be drawn connecting adjacent circles, the projection of a line segment between the center point of each circle and the tangent line can be defined as $\vec{r}$. An angle between the $\vec{d}$ and $\vec{r}$ can be notated as α. The intersection point (x'_k, z'_k) can then be derived from Eqns. 3-11 and 3-12 using the supplementary angle theorem (Eqn. 3-10) to find γ. These points are joined to complete the wavefront. From the completed wavefront a new set of point sources is created at regular intervals and the process is repeated.

$$\gamma = 180 - (\alpha + \beta) \qquad \textit{Eqn. 3 - 10}$$

$$x'_k = x_k + \|r_k\|\sin(\gamma) \qquad \textit{Eqn. 3 - 11}$$

$$z'_k = z_k + \|r_k\|\cos(\gamma) \qquad \textit{Eqn. 3 - 12}$$

3.4 Fast Marching Method

Using a similar method, the expanding GPR wavefront can be modelled directly from the Eikonal Equation using finite-difference schemes. These are computational techniques that numerically approximate the solution of a boundary-value partial differential equation. The most common technique used in geological tomography is the Fast Marching Method (FMM). The algorithm tracks the spreading pattern of a propagating interface from a known starting point (Sethian, 1998). Conceptually, it is similar to the way wildfire might spread through a field of dry brush. From a single point of ignition, the fire spreads only to the areas adjacent to the burning front. The spreading rate can be variable and dependent

upon several external factors. However, once an area has been burned, there is no longer fuel for re-ignition, which is stated in FMM terminology as satisfying the entropy condition.

The solution is a continuous surface in an x-y plane that is propagating normal to itself. As the surface moves along its axis, the object intersects the x-y plane forming a two-dimensional interface. The coordinates of this expanding front are calculated from first arrival time T(x,y) as the curve crosses each point on the plane. The forward motion of the surface characterizes the solution to the boundary value problem. By stating the velocity in terms of position along the axes, such that in one-dimension the change in length can be found as dx = F dt, and by taking the spatial derivate along the x-y plane, the equation reduces to Eqn. 3-13, the Eikonal Equation (Gremaud and Kuster, 2004).

$$|\nabla T|F = 1 \qquad \textit{Eqn. 3 - 13}$$

The difficultly in solving this equation is that it requires the surface to be a smooth, continuous, and differentiable function. Actual field data rarely meets this criteria. Following Sethian (1998), a weak solution to the system may exist using the Hamilton-Jacobi viscosity equations. By applying the Euler-Lagrange differential equation to Fermat's principle and Snell's law, the Hamilton-Jacobi Equation (HJE) is developed by applying calculus of variations methods. Eqn. 3-14 is the resulting general partial differential equation.

$$\alpha u_t + H(D_u, x) = 0 \qquad \textit{Eqn. 3 - 14}$$

Where:

D_u represents the partials of each axis.

In the case of the Eikonal equation, α is zero and the function H is reduced to $H = |\nabla\Omega|F$. The system can be further simplified by restricting the boundary value perspective of the plane to expanding fronts that only move in one direction. In other words, the radar velocity must be greater than zero for all points. This is a reasonable assumption in GPR tomography. From this restriction, it is guaranteed that

there can be no more than a single crossing at any time T for each point, thus satisfying the entropy condition. The entropy condition is added to the modified Hamilton-Jacobi equation (Eqn. 3-15) as a smoothing parameter (Sethian, 1998).

$$F|\nabla\Omega| \approx F|\nabla u + \epsilon\nabla^2 u| \qquad \textit{Eqn. 3 - 15}$$

Instead of creating an additional unknown parameter for viscosity (ϵ), Chacon and Vladimidsky (2011) suggested analyzing the behavior of the system against possible test functions that approximate u. Thus, by creating a smooth test function U, the differentiation is passed from u to U using integration by parts. The approximate solution of u can then be found from the smooth function U by taking the viscosity limit of ϵ as it approaches zero. The method for selecting appropriate test conditions relies on first-order finite-difference schemes (Eqn. 3-16) to the approximate the partial derivatives from points on the surface u. Eqn. 3-17 is then developed by applying the finite-difference schemes (Eqn. 3-16) to the Hamilton-Jacobi Equation (Eqn. 3-15).

$$D_{i,j}^{\pm x}U = \frac{u_{i\pm1,j}-u_{i,j}}{\pm h} \;\; ; \;\; D_{i,j}^{\pm y}U = \frac{u_{i,j\pm1}-u_{i,j}}{\pm h} \qquad \textit{Eqn. 3 - 16}$$

$$\left[\max\left(D_{ij}^{-x}, D_{ij}^{+x}, 0\right)^2 + \max(D_{ij}^{-y}, D_{ij}^{+y}, 0)^2\right]^2 = {}^{1}\!/_{F_{ij}^2} \qquad \textit{Eqn. 3 - 17}$$

The quadrant equations (Eqn. 3-18 and 3-19) are replaced by the smallest of the one-sided updates following the derivation by Malladi et al. (1996).

$$U_H = \min(u_{i\pm1,j}) \qquad \textit{Eqn. 3 - 18}$$

$$U_V = \min(u_{i,j\pm1}) \qquad \textit{Eqn. 3 - 19}$$

The solution for the approximate surface U is found from Eqns. 3-20 or 3-21. If the one-sided updated for the quadrant parameters meets the constraint $|U_H - U_V| \leq {}^{h}\!/_{F_{ij}}$, then a solution exists for

Eqn. 3-20 and it the equation is a valid approximation. If this constraint is not satisfied then no solution exists for Eqn. 3-20, then Eqn. 3-21 is used to approximate the point along the surface (Chacon and Vladimidsky, 2011)

$$U_{ij} = \frac{U_H + U_V}{2} + \frac{1}{2}\sqrt{(U_H + U_V)^2 - 2(U_H^2 + U_v^2 - {h^2}/{F_{ij}^2})} \qquad \textit{Eqn. 3 - 20}$$

$$U_{ij} = \min(U_H, U_V) + {h}/{F_{ij}} \qquad \textit{Eqn. 3 - 21}$$

The function U can then be found by setting all nodes to infinity except the starting location where U_0=0. The next step is to find expected values for the system as $\overline{U}$. If the value of $\overline{U}$ is less than the current value of U_{ij}, then the expected values are set as the current value. This process is repeated until the solution is stable, or $\overline{U} = U_{ij}$ for all cells. Although, this method will arrive at an appropriate approximation of the boundary value function u; it is computationally inefficient. From the entropy condition, the information can travel in one direction only, which is from smaller values of U to larger values U. Once a value has been calculated as its smallest possible value, it cannot be recalculated. Therefore, only those values with a narrow band around the front are calculated. Thus the speed of the algorithm can be greatly improved by limiting the computation to a sub-set of values around the existing front, called a Narrow-Band Set (Sethian, 1998). Following each step, the solved points are “frozen”, or prohibited from changing, and new points are added to the narrow band; while the distant points remain untouched. This significantly reduces the number of cells the algorithm needs to compute for each iteration.

3.5 Huygens’ Wavefront Expansion

Huygens' wavefront expansion further improves upon the finite difference solution to the Eikonal equation by incorporating techniques from raytracing. Unlike the Fast Marching Method, Huygens’

Wavefront Expansion is formulated in the ray coordinate system. The wavefront expands as a propagating interface similar to the Fast Marching Method. However, instead of using adjacent nodes to develop the next point, Huygens' wavefront expansion uses adjacent rays. From Huygens' principle, each point on a wavefront is a source of secondary wavelets. The goal is to keep track of these wavelets, through ray tracing, from the original point source. Each ray is parameterized through a parameter γ, often assigned to the initial ray angle and ray length (τ). The family of wavelets can be aggregated into a wavefront similar to Wavefront Construction (Sava and Fomel, 1997).

Using a system of partial differential equations the wavefront can be propagated through the media by stepping forward a collection of rays to discrete time steps. First, the Eikonal equation is expanded into its spatial derivatives (Eqns. 3-22 and 3-23).

$$|\nabla u|^2 = {}^1\!/_{v^2} \qquad \textit{Eqn. 3 - 22}$$

$$\left(\frac{\partial \tau}{\partial x}\right)^2 + \left(\frac{\partial \tau}{\partial z}\right)^2 = {}^1\!/_{v_{x,y}^2} \qquad \textit{Eqn. 3 - 23}$$

To simplify working in a Cartesian grid, these systems are transformed by Eqn. 3-24 to substitute the ray parameters τ and γ for the inverse functions in terms of x and z.

$$\left(\frac{\partial x}{\partial \tau}\right)^2 + \left(\frac{\partial z}{\partial \tau}\right)^2 = v^2(x_{\tau,\gamma}, z_{\tau,\gamma}) \qquad \textit{Eqn. 3 - 24}$$

Eqn. 3-25 shows the discrete form of the equation following a first-order finite-difference scheme.

$$(x_{j+1}^i - x_j^i)^2 + (z_{j+1}^i - z_j^i)^2 = (r_j^i)^2 \qquad \textit{Eqn. 3 - 25}$$

Where:

$$i = \gamma$$
$$j = \tau$$
$$r_j^i = v_j^i \Delta\tau$$

As stated in Eqn. 3-26, γ is defined as a function of the spatial coordinates such that the rays are locally orthogonal to the isochomatic wavefronts in terms of τ (Sava and Fomel, 1997). A family of Huygens spheres can then be centered at arbitrary points along the wavefront for each step. The ray parameter (γ) is used to distinguish the unique Huygens source; generalized as Eqn. 3-27 following Zhang (1993).

$$\frac{\partial \tau}{\partial x}\frac{\partial \gamma}{\partial x} + \frac{\partial \tau}{\partial z}\frac{\partial \gamma}{\partial z} = 0 \qquad \textit{Eqn. 3 - 26}$$

$$[x - x(\gamma)]^2 + [z - z(\gamma)]^2 = r^2(\gamma) \qquad \textit{Eqn. 3 - 27}$$

The next wavefront is derived from the envelope of the family of Huygens Spheres. To find the envelope Eqn. 3-27 is differentiated in terms of the Huygens family parameter (γ), shown in Eqn. 3-28. Then the γ-derivates are translated into a centered finite-difference scheme (Eqn. 3-29).

$$[x(\gamma) - x]x'(\gamma) + [z(\gamma) - z]z'(\gamma) = r(\gamma)r'(\gamma) \qquad \textit{Eqn. 3 - 28}$$

$$\left(x_j^i - x_{j+1}^i\right)\left(x_j^{i+1} - x_j^{i-1}\right) + \left(z_j^i - z_{j+1}^i\right)\left(z_j^{i+1} - z_j^{i-1}\right) = r_j^{i+1}(r_j^{i+1} - r_j^{i-1}) \qquad \textit{Eqn. 3 - 29}$$

The two finite-difference schemes can be combined and re-arranged to solve for the next wavefront for each ray parameter (Eqns. 3-30 and 3-31).

$$x_{j+1}^i = x_j^i - r_j^i[\alpha\left(x_j^{i+1} - x_j^{i-1}\right) \pm \beta\left(z_j^{i+1} - z_j^{i-1}\right)] \qquad \textit{Eqn. 3 - 30}$$

$$z_{j+1}^i = z_j^i - r_j^i[\alpha\left(z_j^{i+1} - z_j^{i-1}\right) \mp \beta\left(x_j^{i+1} - x_j^{i-1}\right)] \qquad \textit{Eqn. 3 - 31}$$

Where the parameters α and β are defined in Eqns. 3-32 and 3-33, respectively.

$$\alpha = \frac{r_j^{i+1} - r_j^{i-1}}{(x_j^{i+1} - x_j^{i-1})^2 - (z_j^{i+1} - z_j^{i-1})^2} \qquad \textit{Eqn. 3 - 32}$$

$$\beta = \pm(x_j^{i+1} - x_j^{i-1})\sqrt{\frac{(x_j^{i+1} - x_j^{i-1})^2 + (z_j^{i+1} - z_j^{i-1})^2 - (r_j^{i+1} - r_j^{i-1})^2}{(x_j^{i+1} - x_j^{i-1})^2 + (z_j^{i+1} - z_j^{i-1})^2}} \qquad \textit{Eqn. 3 - 33}$$

The scheme needs to be initialized with one complete wavefront around the point source and two boundary rays from the minimum/maximum initial ray angles γ. Given these boundary conditions the finite-difference model will update the solution fields to solve for the unknown ray parameters. The wave propagation can then be shown on the cross-section as a travel time surface, or isochrone contours (Nowack, 1992).

3.6 Chapter Summary

Raytracing allows the computation of GPR tomography by defining the path by which electromagnetic waves traverse through the media. This chapter discusses the two common families of raytracing techniques: raypath and wavefront. Raypath techniques are derived from Fermat's principle of least time to idealize the wave propagation as a quasi-linear path. The straight ray assumption is that the ray travels in a straight line from the source to the receiver. However, this is only valid for homogeneous media. For inhomogenous media, the curved ray assumption is appropriate. It uses Snell's law to reflect or refract the rays at the interface between two different materials. Two methods of raytracing with curved ray raypath techniques are described: Geometric raytracing and Gaussian raytracing. The methods are similar and differ only in the way which radar velocity is calculated. Geometric raytracing uses the radar velocity for adjacent cells alone, while Gaussian raytracing applies a weighted average for several cells perpendicular to the raypath. Wavefront techniques are numerical approximations the Eikonal equation. Two methods are considered: NORSAR wavefront construction and Fast the Marching Method. NORSAR wavefront construction propagates the wavefront by assuming that points at regular intervals along the envelope are sources of secondary waves, which can be used to develop the next wavefront. Fast Marching Method starts at the transmitter location and steps cell-by-cell in an iterative procedure. The final method discussed is Huygen's Wavefront Expansion, where several raypaths at several starting angles are passed through the media. This information is then used to build wavefronts.

Chapter 4

INVERSION SCHEMES

The path electromagnetic waves follow through a media is dependent upon the material's electromagnetic properties, specifically radar velocity. In tomography, these properties are usually not known and must be calculated from known boundary conditions. To begin, a radar velocity is assumed and raytraced. The deviation between the expected and calculated values leads to a correction of the radar velocity. This process is repeated until satisfactory. In general, tomography involves large, sparse matrices that are often severely ill-conditioned with measurement errors inherit in field data (Kabanikhin, 2008). Due to limitation of computer memory and numerical inaccuracies, iterative methods are usually used to solve the systems (Rao, 2002). In this thesis three methods are discussed: Ordinary Least Squares, Conjugate Gradient, and LSQR. Ordinary Least Squares determines the solution by minimizing the squared-error between the observed and calculated boundary conditions. Conjugate Gradient refines Ordinary Least Squares by determining the magnitude and direction of the next step toward minimizing the error. Such that fewer iterations are needed to arrive at a solution. LSQR refines Conjugate Gradient for non-linear problems using similar techniques of orthogonal search directions and minimizing the squared error. However, it takes advantage of the QR factorization to reduce the iterations needed to solve severely ill-conditioned problems.

4.1. Inverse Problem

A forward problem finds a function to describe the physical field at any point within a given domain where material properties are known. An inverse problem uses the known function of the physical field to reconstruct the unknown material properties using known boundary conditions. These

known boundary conditions are often obtained from field measurements and are subject to measurement error (however small). For example, slight errors can occur in the vertical placement of the antenna, inaccurate first arrival travel time selection, or approximation errors from the discretization of the formation into a regularized grid. Even though these errors account for a small portion of the total error under the simplistic straight ray raypath assumption. When the model is advanced to the more accurate curved ray raypath and wavefront methods small errors can propagate through the system having significant effects on the solution matrix (Cerveny et al., 2012).

Each ground penetrating radar (GPR) measurement corresponds to a single ray traversing through the media. Under this model there are many more cells that do not interact with the individual ray path for each observation than affected cells, often forming large sparse matrices. Due to the quasi-linear path each ray can take, even ray coverage is not guaranteed. For example, the cells in the center of the solution matrix will have many more rays passing through than the corners. Therefore, often more observations are required than cells, creating an over-determined system.

4.1.1 Newton's Method

Over-determined systems with uncertain measurement errors are not guaranteed to converge to a solution, nor are they limited to a single solution. Due to the resources needed to solve large, sparse systems, they are often impractical to solve using direct substitution methods (Rao, 2002). However, if each unknown coefficient is considered a potential degree of freedom constrained by each known equation; an approximate solution for the system can be found iteratively. The system can converge to the most likely solution by making slight corrections to minimize the residual, or the discrepancy between the calculated and measured solution vectors. Such techniques solve a system of equations by assuming an initial guess then perturbing the coefficient matrix to reduce the residual. The process is repeated until the system converges to satisfy a pre-set threshold, or a maximum number of iterations has been reached to halt the divergence of the system.

While an exact solution may not exist, there may be a nearly exact solution. Given the system $Ax=b$, where x is not exact and the observed b_o differs slightly from the model b_n due to measurement and discretization errors, the solution vector x can be improved by setting the measured data equal to the calculated data (Eqn. 4-1) and calculating the residual using Eqn. 4-2 (Rao, 2002).

$$Ax_n - b_n = Ax_{n+1} - b_o \qquad \textit{Eqn. 4 - 1}$$

$$A(x_n - x_{n+1}) = b_n - b_o$$

$$(x_n - x_{n+1}) = A^{-1}(b_n - b_o)$$

$$\Delta x = A^{-1}(Ax_n - b_o) \qquad \textit{Eqn. 4 - 2}$$

The solution vector for next iteration is defined by subtracting the residual solution vector from the model vector using Eqn. 4-3. It is repeated until the stopping criteria, often a minimum residual, is satisfied. This is often referred to as Newton's Method, or the error correction method (Rao, 2002).

$$x_{n+1} = x_n - \Delta x \qquad \textit{Eqn. 4 - 3}$$

4.1.2 Ordinary Least Squares

The approximate solution can be determined by minimizing the difference of the solution vector between iterations. A common approach is to use the sum of the squares for the error vector, or L-2 norm. The error term can be expressed as the difference between the calculated data vector and the observed data vector (Eqn. 4-4), which can be transformed to Eqn. 4-5.

$$e = b_n - b_o \qquad \textit{Eqn. 4 - 4}$$

$$e = (Ax - b) \qquad \textit{Eqn. 4 - 5}$$

Minimizing a system by the sum of the squared error vector is formally called Ordinary Least Squares (OLS). It is a method to estimate the model parameters that provide the best fit, or least error, between the model estimate and the field data. The discrepancy is then squared to weigh, or assign a higher cost to, larger errors over smaller errors. For example, in real systems field data rarely matches the expected modeled data with perfect accuracy. The results are expected to have a (hopefully small) independent and identically distributed error component. Models are a simplification of reality. It is unlikely to capture every factor influencing the resultant data, but often several principal components can adequately define the system. Therefore, a small degree of variability is acceptable. The OLS method assigns smaller weights to these effects; relying on the L-2 Norm of the matrix. Since points further away are assigned a larger penalty, outliers will skew the model. Using the L-2 norm, the OLS system can be solved in matrix form by expanding the squared error (Eqn. 4-6) to Eqn. 4-7.

$$\begin{aligned} \|Ax-b\|_2^2 &= e^T e && \textit{Eqn. 4 - 6} \\ &= (Ax-b)^T(Ax-b) \\ &= A^T x^T Ax - A^T x^T\, b - b^T Ax + b^T b \\ &= A^T x^T Ax - 2b^T Ax + b^T b && \textit{Eqn. 4 - 7} \end{aligned}$$

Eqn. 4-8 is developed from the surface of the squared error, the minima can be found by setting the first derivative of Eqn. 4-7 to zero and solving for model parameter, x.

$$\begin{aligned} 0 &= (A^T x^T Ax - 2b^T Ax + b^T b)\, {}^{\partial}/_{\partial x} \\ 0 &= 2A^T Ax - 2A^T b \\ A^T Ax &= A^T b \\ x &= (A^T A)^{-1} A^T b && \textit{Eqn. 4 - 8} \end{aligned}$$

Unstable systems, such that a small change in the coefficient matrix causes a large change in the calculated solution vector, are known as ill-conditioned systems. In other words, systems where the ratio between the relative error of the solution vector and the relative error of the coefficient matrix is proportional to the relative stability, or condition, of the system. For example, Eqn. 4-9 Is derived from the system $Ax=b$ and with slight perturbation of that system $A'x'=b$.

$$Ax \approx A'x' \qquad \textit{Eqn. 4 - 9}$$

Where the change in the system (ΔA and Δx) can be described from Eqns. 4-10 and 4-11 using the perturbations of Eqn. 4-9.

$$\Delta A = A' - A \qquad \textit{Eqn. 4 - 10}$$

$$\Delta x = x' - x \qquad \textit{Eqn. 4 - 11}$$

By combining Eqns. 4-10 and 4-11 with the assumption stated in Eqn. 4-9, the system can be algebraically rearranged to Eqn. 4-12. The change in x is then in terms of the other components of the linear system (Eqn. 4-13).

$$Ax = (\Delta A + A)(\Delta x + x) \qquad \textit{Eqn. 4 - 12}$$

$$Ax = \Delta A\Delta x + \Delta Ax + \Delta xA + Ax$$

$$0 = \Delta A(\Delta x + x) + \Delta xA$$

$$-\Delta xA = \Delta A(\Delta x + x)$$

$$\Delta x = -A^{-1}\Delta A(\Delta x + x) \qquad \textit{Eqn. 4 - 13}$$

Eqn. 4-14 performs the uniform matrix norm of Eqn. 4-13, which can be used to measure the least absolute error. The equation is then rearranged to illustrate the relationship between a change in the x

parameter in terms of the change in the A parameter (Eqn. 4-15). These relative changes can be assigned to the scalar κ, often referred to as the condition number, and used to determine the condition, or stability, of the system by calculating Eqn. 4-16. Combined with machine precision it allows one to set an upper bound on the adequacy of the solution.

$$\|\Delta x\| \leq \|A^{-1}\|\|\Delta A\|\|(\Delta x + x)\| \quad \textit{Eqn. 4 - 14}$$

$$\|A\|\|\Delta x\| \leq \|A^{-1}\|\|\Delta A\|\|(\Delta x + x)\|\|A\|$$

$$\frac{\|\Delta x\|}{\|(\Delta x + x)\|} \leq \|A^{-1}\|\|A\| \frac{\|\Delta A\|}{\|A\|}$$

$$\frac{\frac{\|\Delta x\|}{\|(\Delta x + x)\|}}{\frac{\|\Delta A\|}{\|A\|}} \leq \|A^{-1}\|\|A\| \quad \textit{Eqn. 4 - 15}$$

$$\kappa = \|A^{-1}\|\|A\| \quad \textit{Eqn. 4 - 16}$$

4.1.3 Regularized Least Squares

Because there may not be a unique solution, inverse problems are often ill-posed (e.g. contain error contaminated data). Additionally, the non-linear characteristics of tomography usually result in ill-conditioned (nearly singular or high condition number) matrices that are sensitive to small changes (Aldridge and Oldenburg, 1993). Therefore, regularization techniques, such as dampening parameters or pre-conditioning, are used to stabilize the equations. Regularized least squares is a collection of techniques used to add additional constraints to ill-posed problems to promote convergence.

4.1.3.1 Tikhonov Regularizing Method

The general approach is the Tikhonov Regularizing Method. The premise is that the collected field data contains the true error-free data, $\hat{b}$, plus an unknown error, e. Solving the linear system of equations using the error-free field data, $Ax = \hat{b}$ is not possible. Tikhovnov regularization aims to find the approximate solution using a penalized, or weighted, least squares problem. Regularization is provided

by the arbitrary regularization matrix, L, and the regularization parameter, γ. Eqn. 4-17 states the L-2 norm, called the regularization term, of the Tikhonov regularization (Zhdanov, 1993). The solution can then be found from the first derivation (Eqn. 4-18) and algebraically rearranged in terms of the solution vector (Eqn. 4-19).

$$min\{\|Ax-b\|_2^2+\gamma\|Lx\|_2^2\} \qquad \textit{Eqn. 4 - 17}$$

$$min\{(Ax-b)^T(Ax-b)+\gamma(Lx)^T(Lx)\}$$

$$min\{A^Tx^TAx-bA^Tx^T-b^TAx+b^Tb+\gamma L^TLx^Tx\}$$

$$\begin{aligned}(A^Tx^TAx-2b^TAx+b^Tb+\gamma L^TLx^Tx)\,{}^{\partial}/_{\partial x} &= 0 \qquad \textit{Eqn. 4 - 18}\\ 2A^TAx-2A^Tb+0+2\gamma L^TLx &= 0\\ x(A^TA+\gamma L^TL) &= A^Tb\\ x &= (A^TA+\gamma L^TL)^{-1}A^Tb \qquad \textit{Eqn. 4 - 19}\end{aligned}$$

The rate of convergence and adequacy of a solution depends on the choice of regularization parameters. L can be any matrix needed to smooth the solution, typically a first-order or second-order finite-difference differentiation matrix is used. However, considerable work can be required to determine the appropriate parameters (Zhdanov 1993).

4.1.3.2 Marquardt-Levenburg Method

For most problems in tomography, the Tikhonov method can be greatly simplified by the special case where L is assumed to be the identity matrix. Under this assumption, the work required to determine the most appropriate solution is confined to a single scalar value (γ). In general, significant improvements in the condition number are realized by increasing the dampening parameter (Figure 4-1). However, the improvements are often costly in terms of convergence (Pujol 2007).

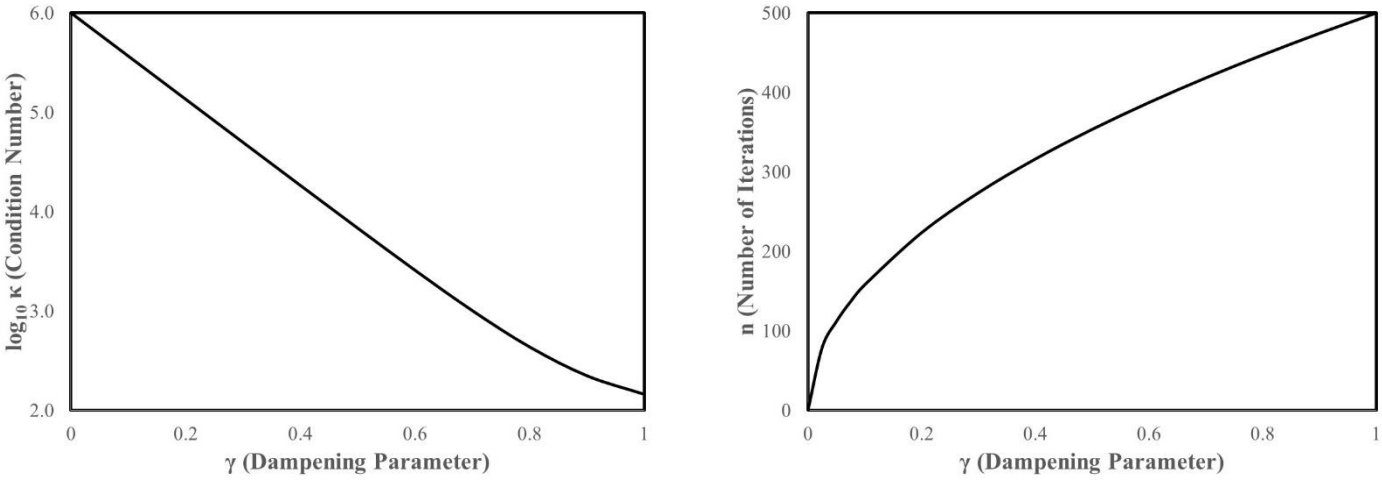

(a) (b)

Figure 4-1, the inverse relationship between the (a) improved condition number and the (b) number of iterations required in terms of the dampening parameter.

4.1.4 Newton Method for Regularized Least Squares

In practice the most common method of using Least Squares to solve problems arising from tomography applications is to use Newton's Method to solve the Marquardt-Levenburg form of the dampened least squares problem. The first step is to initialize an error matrix, J, with the expected values based on a priori knowledge (Eqn. 4-20). The regularized least-squares method is then applied to calculate the difference between the solution to the system and the a priori assumption (Eqn. 4-21), then adjusting the model parameters and repeating until the difference in x is small (Eqn. 4-22).

$$J = Ax_n - b \qquad \text{Eqn. 4 - 20}$$

$$\Delta x = (A^T A + \gamma I)^{-1} A^T J \qquad \text{Eqn. 4 - 21}$$

$$x_{n+1} = x_n - \Delta x \qquad \text{Eqn. 4 - 22}$$

The residual is expected to approach zero with increasing iterations. However, inaccuracies in the solution matrix, such as those caused by round-off error in large matrices may cause the residual to grow asymptotically, a condition known as divergence (Kabanikhin 2008). Additional stopping criteria is needed

to detect and halt divergence. Typically, a maximum number of iterations is specified. If the algorithm has not found a significantly small residual by the maximum iteration an error code is returned.

4.2 Conjugate Gradient Method

Ordinary Least Squares solves most ill-posed systems. However, for large, sparse matrices the rate of convergence can be slow. The reason is that OLS gives the "direction" of the solution by solving for the residual term. It does not, however, give the size of the step needed allowing the algorithm over-shoot the solution. The dampening parameter improves these results by providing a scalar valve to adjust the magnitude of the step, yet it is a constant. The method of Conjugate Gradient was developed by Hestenes (1973) to recalculate the step size each iteration.

4.2.1 Steepest Descent

For linear problems, the solution generally takes the quadratic form (Eqn. 4-23).

$$f_x = ½x^T Ax - b^T + c \qquad \textit{Eqn. 4 - 23}$$

Where

A is the "problem" matrix,

b is the "solution" vector,

x is the vectorized "coefficient" matrix, and

c is a scalar constant.

If the matrix A is symmetrical and positive-definite, the solution will take a parabolic form without saddle points or local minima. A single solution (Eqn. 4-25) can be found by setting the gradient of the quadratic function to zero (Eqn. 4-24).

$$\nabla f_x \quad = \quad 0 \qquad \textit{Eqn. 4 - 24}$$

$$
\begin{aligned}
(½x^T Ax - b^T + c)\frac{\partial}{\partial x} &= 0 \\
(½xA^T + ½xA - b) &= 0 \\
½(A^T + A)x &= b \qquad (A = A^T) \\
Ax &= b \qquad \textit{Eqn. 4 - 25}
\end{aligned}
$$

The residual (Eqn. 4-26) can then be defined as the difference between the expected solution vector b and the calculated solution Ax.

$$r_i = b - Ax_i \qquad \textit{Eqn. 4 - 26}$$

By inspection, the residual is in the direction opposite of the gradient$-\nabla f_x = r_i$. Conceptually, the residual can be thought of as the direction of the steepest descent. Therefore, the next iteration x_{i+1} would be a step from the current location x in the direction of the steepest descent: $x_{i+1} = x_i + \alpha r_i$. Yet, the magnitude of the step is unknown. It is expected to fall on the planar surface defined by the residual. Thus, the solution can be limited to the values at the intersection of the quadratic function and the residual. Because of the initial assumptions about the function, the shape of the intersection will be parabolic. The minimum value is found by first setting the direction derivative of the function to zero (Eqn. 4-27).

$$
\begin{aligned}
\frac{\partial}{\partial \alpha} f_{(x_{i+1})} &= 0 \qquad \textit{Eqn. 4 - 27} \\
f'_{(x_{i+1})} \frac{\partial}{\partial \alpha} x_{i+1} &= 0 \\
f'_{(x_{i+1})} x_i &= 0
\end{aligned}
$$

This technique is often called "*line search"* in the literature (Shewchuk, 1994). The projection of the gradient vector on the intersecting line represents the rate of increase along the line. At the point with no rate of increase, the directional derivative will be zero. Note there will not be a projection at this location, therefore the minimum point will also be orthogonal. From this assumption, the magnitude of the step is defined using α (Eqn. 4-28).

$$
\begin{aligned}
{f_{(x_{i+1})}}^T r_i &= 0 \\
{r_{i+1}}^T r_i &= 0 \\
(b - Ax_{i+1})^T r_i &= 0 \\
(b - A(x_i + \alpha r_i))^T r_i &= 0 \\
(b - Ax_i + \alpha A r_i)^T r_i &= 0 \\
(b - Ax_i)^T r_i + (\alpha A r_i)^T r_i &= 0 \\
(b - Ax_i)^T r_i &= (\alpha A r_i)^T r_i \\
{r_i}^T r_i &= (\alpha A r_i)^T r_i \\
\alpha &= \frac{{r_i}^T r_i}{{r_i}^T A r_i}
\end{aligned}
\qquad \textit{Eqn. 4 - 28}
$$

4.2.2 Conjugate Directions

Steepest descent often calculates several steps in the same direction, which can be slow to converge. The convergence can be improved by modifying the algorithm to take exactly one step in each search direction using the method of conjugate direction. This method picks a set of orthogonal search directions, d, and calculates exactly one step for each direction. This can be accomplished by setting the next error term e_{i+1} orthogonal to the search direction d_i such that $d_i^T e_{i+1} = 0$. Then taking step a toward the next error term $e_{i+1} = e_i + \alpha d_i$. Using these conditions, α is the size of each step (Eqn. 4-29).

$$
\begin{aligned}
d_i^T e_{i+1} &= 0 \\
d_i^T (e_i + \alpha d_i) &= 0 \\
\alpha &= -\frac{d_i^T e_i}{d_i^T d_i}
\end{aligned}
\qquad \textit{Eqn. 4 - 29}
$$

Yet, to finding the magnitude of the step (α), requires knowledge of the search direction and the error term. However, if the error term was known, the solution would be known. Therefore, without knowing the error the problem cannot be solved. The solution is to make the search directions A-orthogonal, known as conjugate, such that $d_i^T A d_j = 0$, and calculating the minimum point similar to the method of steepest descent. However, instead of performing a line search the minimum point along each search direction is found by setting the directional derivative to zero.

$$
\begin{aligned}
{}^{\partial}/_{\partial \alpha}\, f(x_{i+1}) &= 0 \\
f'(x_{i+1})\, {}^{\partial}/_{\partial \alpha}\, x_{i+1} &= 0 && \text{(chain rule)} \\
-r_i^T d_i &= 0 && ;\ (f'(x_i) = -r_i) \\
d_i^T A e_{i+1} &= 0 && ;\ (r_i = -A e_i) \\
d_i^T A (e_i + \alpha d_i) &= 0 \\
\alpha_i &= -\frac{d_i^T A e_i}{d_i^T A d_i} \\
\alpha_i &= \frac{d_i^T r_i}{d_i^T A d_i} && ;\ (r_i = -A e_i)
\end{aligned}
$$

4.2.3 Gram-Schmidt Process

With the error term eliminated, a set of orthogonal search directions d_i can be found using the *conjugate* Gram-Schmidt process. From a set of linearly independent vectors u_i a set of mutually conjugate vectors can be found. To construct d_i, any components not A-orthogonal to the previous vectors d_{i-1} can be subtracted from the u_i vector (Eqn. 4-30).

$$
\begin{aligned}
d_0 &= u_0 \\
d_1 &= u_1 - \beta_{10} d_0 \\
d_2 &= u_2 - \beta_{10} d_0 - \beta_{21} d_1 \\
&\vdots \\
d_i &= u_i + \sum_{k=0}^{i-1} \beta_{ik}\, d_k
\end{aligned}
\qquad \textit{Eqn. 4 - 30}
$$

Because the search directions are conjugate, the equation is further simplified by pre-multiplying the expression by the inner product of $d_j^T A$ to eliminate all but a single β valve (Eqn. 4-31).

$$
\begin{aligned}
d_i^T A d_j &= u_i^T A d_j + \sum_{k=0}^{i-1} \beta_{ik} d_k^T A d_j \\
i > j \qquad 0 &= u_i^T A d_j + \beta_{ij} d_j^T A d_j \qquad ;\ (d_i^T A d_j = 0) \\
\beta_{ij} &= -\frac{u_i^T A d_j}{d_j^T A d_j}
\end{aligned}
\qquad \textit{Eqn. 4 - 31}
$$

Even with a solvable expression, there is still a practical limitation. The computation cost of maintaining the previous search directions in memory may not be possible for large systems, which are common in tomography (Shewchuk, 1994).

4.2.4 Conjugate Gradient

The error term (Eqn. 4-32) as a linear combination of the search direction, where the magnitude of the error is δ_i.

$$
e_i = \sum_{j=i}^{n-1} \delta_j d_j \qquad \textit{Eqn. 4 - 32}
$$

By adding a term, $-d_i^T A$, to each side of Eqn. 4-32, the transpose of the ith search direction times the jth residual is naught (Eqn. 4-33).

$$\begin{aligned} -d_i^T A e_j &= -\sum_{j=i}^{n-1} \delta_j d_i^T A d_j \\ -d_i^T A e_j &= 0 \qquad ; (d_i^T A d_j = 0) \\ d_i^T r_j &= 0 \end{aligned} \qquad \textit{Eqn. 4 - 33}$$

By taking the inner product of the Gram-Schmidt process (Eqn. 4-30) and the residual vector r_j, Eqn.4-34 can be further reduced (Eqn. 4-35)

$$d_i^T r_j = u_i^T r_j + \sum_{k=0}^{i-1} \beta_{ik} d_k^T r_j \qquad \textit{Eqn. 4 - 34}$$

$$0 = u_i^T r_j + 0 \qquad \textit{Eqn. 4 - 35}$$

The error is orthogonal to all previous search terms (Strang, 2007). Since $r_i = -Ae_i$, it can be concluded that the residual is also orthogonal to the previous search terms. Therefore, by modifying conjugate directions where the search directions are found by conjugating the residuals such that $u_i = r_i$. Each new residual is then simply a linear combination of the previous residual and Ad_i (Eqn. 4-36). It is created by repeatedly applying a matrix to a vector. This type of structure is often called a Krylov subspace (Strang, 2007).

$$\begin{aligned} r_{i+1} &= -Ae_{i+1} \\ &= -A(e_i + \alpha_i d_i) \\ &= r_i - \alpha_i A d_i \end{aligned} \qquad \textit{Eqn. 4 - 36}$$

The new subspace $\mathcal{D}_{i+1}$ is formed from the union of the previous subspace $\mathcal{D}_i$ and the subspace $A\mathcal{D}_i$. The Krylov subspace contains all combinations of $\mathcal{K} = \{b \quad Ab \quad A^2b \quad \ldots\}$ and a Krylov Matrix would consist of the combinations of $\mathcal{K}$ that best approximate the original equation. The Conjugate Gradient finds the Krylov matrix where the residual is orthogonal to $\mathcal{K}$ for $d_{i-1} \in \mathcal{D}_i$. Because $A\mathcal{D}_i$ is included in $\mathcal{D}_{i+1}$ and $r_{i+1}$is orthogonal to $\mathcal{D}_{i+1}$, we can state that r_{i+1} is conjugate to $\mathcal{D}_i$. The Gram-Schmidt conjugate can then be derived in terms of the residual only. Eqn. 4-37 states the inner product of r_i and r_{j+1}.

$$r_{j+1} = r_j - \alpha_j A d_j \qquad \textit{Eqn. 4 - 37}$$

$$r_i^T r_{j+1} = r_i^T r_j - \alpha_j r_i^T A d_j$$

$$\alpha_j r_i^T A d_j = r_i^T r_j - r_i^T r_{j+1}$$

$$\alpha_j r_i^T A d_j = 0 - r_i^T r_{j+1} \qquad ; (r_i^T r_j = 0)$$

$$r_i^T A d_j = -\frac{r_i^T r_i}{\alpha_{i-1}} \qquad ; (i = j + 1)$$

$$d_j^T A d_j \beta = \frac{r_i^T r_i}{\alpha_{i-1}} \qquad ; (\beta = -\frac{r_i^T A d_j}{d_j^T A d_j})$$

$$\beta = \frac{1}{\alpha_{i-1}} \frac{r_i^T r_i}{d_{i-1}^T A d_{i-1}} \qquad \textit{Eqn. 4 - 38}$$

Eqn. 4-38 is further simplified by substituting the previously defined step size α for each search direction d_i and applying the identity $d_i^T r_i = u_i^T r_i$. Eqn. 4-39 does not require storing all the previous search directions, just a single vector for the previous residual.

$$
\begin{aligned}
\beta &= \frac{1}{\alpha_{i-1}} \frac{r_i^T r_i}{d_{i-1}^T A d_{i-1}} && ; (\alpha_i = \frac{d_i^T r_i}{d_i^T A d_i}) \\
\beta &= \frac{d_{i-1}^T A d_{i-1}}{d_{i-1}^T r_{i-1}} \frac{r_i^T r_i}{d_{i-1}^T A d_{i-1}} \\
\beta &= \frac{r_i^T r_i}{d_{i-1}^T r_{i-1}} \\
\beta &= \frac{r_i^T r_i}{d_{i-1}^T r_{i-1}} && ; (d_i^T r_i = u_i^T r_i) \\
\beta &= \frac{r_i^T r_i}{u_{i-1}^T r_{i-1}} && ; (u_i = r_i) \\
\beta &= \frac{r_i^T r_i}{r_{i-1}^T r_{i-1}} && \textit{Eqn. 4 - 39}
\end{aligned}
$$

By considering the magnitude and the direction of the next step towards the solution, conjugate gradient is expected to converge in less iterations than OLS. However, Conjugate Gradient as described is strictly designed for linear, positive-definite matrices. A condition that cannot be guaranteed. Therefore, improved methods for non-linear general matrices is considered.

4.3 LSQR Method: Least-Squares QR Factorization

Paige and Saunders (1982) proposed using an iterative method to solve $Ax = b$ from the least square solution $_{min}\|Ax - b\|_2$ using QR factorization. This method is analytically equivalent to the method of conjugate gradients but relies on a Golub-Kahan bidiagonalization procedure and a Givens Rotation or Householder Method instead of the Gram-Schmidt. It has been shown to reduce memory usage for sparse matrices and produce a more accurate solution in fewer iterations for moderately to severely ill-conditions systems (Paige and Saunders 1982).

4.3.1 Lanczos Reduction to Tridiagonal Form

The motivation for LSQR follows from the Lanczos process (Eqn. 4-40 and 4-41), which is an iterative method to find an orthogonal matrix V_k such that $AV_k = V_k T$.

$$\beta_i v_i = b \qquad \text{Eqn. 4 - 40}$$

$$\left.\begin{aligned} \omega_i &= Av_i - \beta_i v_{i-1} \\ \alpha_i &= v_i^T \omega_i \\ \beta_{i+1} v_{i+1} &= \omega_i - \alpha_i v_i \end{aligned}\right\} i = 1,2,\ldots \qquad \text{Eqn. 4 - 41}$$

After k iterations, the procedure is shown to be Eqn. 4-42 (Paige and Saunders 1982).

$$AV_k = V_k T_k + \beta_{k+1} v_{k+1} e_k^T \qquad \text{Eqn. 4 - 42}$$

Where $V_k \equiv [v_1, v_2, \ldots, v_k]$ and T_k is a tridiagonal matrix in the form of Eqn. 4-43.

$$T_k = \begin{bmatrix} \alpha_1 & \beta_1 & & & \\ \beta_1 & \alpha_2 & \beta_2 & & \\ & \beta_2 & \alpha_3 & \ddots & \\ & & \ddots & \ddots & \beta_n \\ & & & \beta_n & \alpha_n \end{bmatrix} \qquad \text{Eqn. 4 - 43}$$

The round-off error ϵ is summarized by the components of $\beta_{k+1} v_{k+1} e_k^T$. Without rounding error $V_k^T V_k = I$ and the process would terminate at $\beta_{k+1} = 0$. By definition $V_k(\beta_1 e_1) = b$, therefore from Eqn. 4-40 x_k and y_k can be defined as Eqns. 4-44 and 4-45.

$$T_k y_k = \beta_1 e_1 \qquad \text{Eqn. 4 - 44}$$

$$x_k = V_k y_k \qquad \text{Eqn. 4 - 45}$$

By multiplying each side of Eqn. 4-42 by y_k, a sequence of vectors (x_k) is derived to solve the system $Ax = b$, in a manner that eliminates y_k (Eqn 4-46).

$$
\begin{aligned}
AV_k y_k &= V_k T_k y_k + \beta_{k+1} v_{k+1} e_k^T y_k \\
AV_k y_k &= V_k T_k y_k + \epsilon \\
AV_k y_k &= V_k \beta_1 e_1 + \epsilon && ; (T_k y_k = \beta_1 e_1) \\
Ax_k &= V_k \beta_1 e_1 + \epsilon && ; (x_k = V_k y_k) \\
Ax_k &= b + \epsilon && ; (V_k \beta_1 e_1 = b) \\
Ax_k &= b + \epsilon && \text{Eqn. 4 - 46}
\end{aligned}
$$

4.3.2 Golub-Kahan Bidiagonalization of starting vector b.

Based on work by Golub and Kahan (1965), the Lanczos process results into two forms of a bidiagonalization. The first form is derived from modifying the starting vector Eqn. 4-40 and developing the recurrence relations stated in Eqns. 4-47 and 4-48.

$$
\left.
\begin{aligned}
\beta_i u_i &= b \\
\alpha_i v_i &= A^T u \\
\beta_{i+1} u_{i+1} &= A v_i - \alpha_i u_i \\
\alpha_{i+1} v_{i+1} &= A^T u_{i+1} - \beta_{i+1} v_i
\end{aligned}
\right\} i = 1,2, \ldots
$$

$$
U_k \equiv [u_1, u_2, \ldots, u_k]
$$

$$
V_k \equiv [v_1, v_2, \ldots, v_k]
$$

$$
B_k \equiv \begin{bmatrix} \alpha_1 & & & \\ \beta_1 & \alpha_2 & & \\ & \beta_2 & \ddots & \\ & & \ddots & \alpha_k \\ & & & \beta_{k+1} \end{bmatrix}
$$

$$
U_{k+1}(\beta_1 e_1) = b \qquad \text{Eqn. 4 - 47}
$$

$$
AV_k = U_{k+1} B_k \qquad \text{Eqn. 4 - 48}
$$

The resulting recurrence relation can then be used to rewrite the residual vector r in terms of the intermediate solution matrix y_k.

$$
r = b - Ax_k
$$

$$= \quad U_{k+1}(\beta_1 e_1) - Ax_k \qquad ; (U_{k+1}\beta_1 e_1 = b)$$

$$= \quad U_{k+1}(\beta_1 e_1) - AV_k y_k \qquad ; (x_k = V_k y_k)$$

$$= \quad U_{k+1}(\beta_1 e_1) - U_{k+1}B_k y_k \qquad ; (AV_k = U_{k+1}B_k)$$

$$r \quad = \quad U_{k+1}(\beta_1 e_1 - B_k y_k)$$

Since U_{k+1} is bounded and orthonormal, the best method to minimize $\|r\|$ is by minimizing $\|\beta_1 e_1 - B_k y_k\|$ using y_k. For ease of calculation, Paige and Saunders (1982) suggest defining a quantity t_{k+1} (Eqn. 4-49). The norm of t_{k+1} (Eqn. 4-50) can be minimized using a dampened least squares approach.

$$t_{k+1} = \beta_1 e_1 - B_k y_k \qquad \textit{Eqn. 4 - 49}$$

$$min\|t_{k+1}\| = min\|\beta_1 e_1 - B_k y_k\| \qquad \textit{Eqn. 4 - 50}$$

4.3.3 Least Squares System

From the standard matrix form of Dampened Least Squares (Eqn. 4-51),

$$min \left\| \begin{bmatrix} A \\ \lambda I \end{bmatrix} x - \begin{bmatrix} b \\ 0 \end{bmatrix} \right\|_2 \qquad \textit{Eqn. 4 - 51}$$

which can then be rearranged in terms of the residual vector r where $r = b - Ax$ (Eqn. 4-52).

$$\begin{bmatrix} I & A \\ A^T & -\lambda^2 I \end{bmatrix} \begin{bmatrix} r \\ x \end{bmatrix} = \begin{bmatrix} b \\ 0 \end{bmatrix} \qquad \textit{Eqn. 4 - 52}$$

The Lanczos tridiagonalization process is applied to this system, after $2k + 1$ iterations it permutates to the form (Eqn. 4-53), Which is simply Eqn. 4-50 with an additional dampening parameter.

$$\begin{bmatrix} I & B_k \\ B_k^T & -\lambda^2 I \end{bmatrix}\begin{bmatrix} t_{k+1} \\ y_k \end{bmatrix} = \begin{bmatrix} \beta_1 e_1 \\ 0 \end{bmatrix}$$

$$\begin{bmatrix} r_k \\ x_k \end{bmatrix} = \begin{bmatrix} U_{k+1} & 0 \\ 0 & V_k \end{bmatrix}\begin{bmatrix} t_{k+1} \\ y_k \end{bmatrix}$$

$$min \left\| \begin{bmatrix} B_k \\ \lambda I \end{bmatrix} y_k - \begin{bmatrix} \beta_1 e_1 \\ 0 \end{bmatrix} \right\|_2 \qquad \textit{Eqn. 4 - 53}$$

4.3.4 Golub-Kahan Bidiagonalization of starting vector A^TB

The second bidiagonalization is then derived from the starting vector $A^T b$. The two bidiagonalizations can then be related using their common orthogonal matrix V_k to develop a matrix identical to the upper triangular R_k obtained from conventional QR factorization of B_k and states as recurrence relations in Eqns. 4-54 and 4-55.

$$\left.\begin{aligned} \theta_i v_i &= A^T b \\ \rho_i p_i &= A v_1 \\ \theta_{i+1} v_{i+1} &= A^T p_i - \rho_i v_i \\ \rho_{i+1} p_{i+1} &= A v_{i+1} - \theta_{i+1} p_i \end{aligned}\right\} i = 1,2, \ldots$$

$$P_k \equiv [p_1, p_2, \ldots, p_k]$$

$$V_k \equiv [v_1, v_2, \ldots, v_k]$$

$$R_k \equiv \begin{bmatrix} \rho_1 & \theta_2 & & & \\ & \rho_2 & \theta_3 & & \\ & & \ddots & \ddots & \\ & & & \rho_{k-1} & \theta_{k-1} \\ & & & & \rho_k \end{bmatrix}$$

$$V_k(\theta_1 e_1) = A^T b \qquad \textit{Eqn. 4 - 54}$$

$$AV_k = P_k R_k \qquad \textit{Eqn. 4 - 55}$$

According to work by Paige and Saunders (1982), R_k is identical to the matrix that would be obtained from the conventional QR factorization of B_k (Eqn. 4-56).

$$Q_k{}^T B_k = \begin{bmatrix} R_k \\ 0 \end{bmatrix} \qquad \textit{Eqn. 4 - 56}$$

4.3.5 QR Factorization

Paige and Saunders (1982) found a computational advantage in using QR factorization to solve Eqn. 4-49 by factorizing B_k and linking the bidiagonalizations (Eqns. 4-47, -48, -54, and -55) through their common orthogonal matrix V_k and R_k (Eqn. 4-57).

$$Q_k[B_k \quad \beta_1 e_1] = \begin{bmatrix} R_k & f_k \\ 0 & \bar{\phi}_{k+1} \end{bmatrix} = \begin{bmatrix} \rho_1 & \theta_1 & & & & \phi_1 \\ & \rho_2 & \theta_2 & & & \phi_2 \\ & & \ddots & \ddots & & \vdots \\ & & & \rho_{k-1} & \theta_{k-1} & \phi_{k-1} \\ & & & & \rho_k & \phi_k \\ & & & & & \bar{\phi}_{k+1} \end{bmatrix} \qquad \textit{Eqn. 4 - 57}$$

Where $Q_k = Q_{k,k+1}, \dots, Q_{2,3}, Q_{1,2}$ is a product of plane rotation designed to eliminate the sub-diagonals $\beta_1, \beta_2, \dots, \beta_k$.

The vectors y_k and t_{k+1} could then be found from Eqns. 4-58 and 4-59 (Paige and Saunders 1982).

$$R_k y_k = f_k \qquad \textit{Eqn. 4 - 58}$$

$$t_{k+1} = Q_k^T \begin{bmatrix} 0 \\ \bar{\phi}_{k+1} \end{bmatrix} \qquad \textit{Eqn. 4 - 59}$$

By combining Eqn. 4-58 with Eqn. 4-45, Eqn. 4-60 is developed. Then by the definition $R_k D_k = V_k$, simplifying Eqn. 4-60 to Eqn. 4-61.

$$x_k = V_k R_k^{-1} f_k \qquad \textit{Eqn. 4 - 60}$$

$$x_k = V_k R_k^{-1} f_k = D_k f_k \qquad \textit{Eqn. 4 - 61}$$

Where $D_k = [d_1 \quad d_2 \quad \dots \quad d_k]$ and d_k defined as Eqn. 4-62 and x_k defined as Eqn. 4-63.

$$d_k = \frac{v_k - \theta_k d_{k-1}}{\rho_k} \qquad \textit{Eqn. 4 - 62}$$

$$x_k = x_{k-1} + d_k \phi_k \qquad \textit{Eqn. 4 - 63}$$

4.3.6 QR Factorization Recurrence Relation

The QR Factorization (Eqn. 4-57) is solved through kth plane rotations to eliminate B_{k+1}, which implies the recurrence relation stated in Eqn. 4-64.

$$\begin{bmatrix} c_k & s_k \\ s_k & c_k \end{bmatrix} \begin{bmatrix} \bar{\rho}_k & 0 & \bar{\phi}_k \\ \beta_{k+1} & \alpha_{k+1} & 0 \end{bmatrix} = \begin{bmatrix} \rho_k & \theta_{k+1} & \phi_k \\ 0 & \bar{\rho}_{k+1} & \bar{\phi}_{k+1} \end{bmatrix} \qquad \textit{Eqn. 4 - 64}$$

where

$\bar{\rho}_1 = \alpha_1$

$\bar{\phi}_1 = \beta_1$

c_k, s_k are non-trivial elements of $Q_{k,k+1}$

$\bar{\rho}_k, \bar{\phi}_k$ are intermediate scalars sub-sequentially replaced by ρ_k, ϕ_k

Since Q_k is not directly required, the algorithm does not need to hold $Q_{k,k+1}$ in memory, it is immediately discarded after use. Negligible work is required to compute $R_k, f_k, \bar{\phi}_{k+1}$ and further improvements are realized by setting $\omega_k = \rho_k d_k$.

4.4 Chapter Summary

This chapter considered three different inversion techniques. Ordinary Least Squares (OLS) determines the best fit, or least squared error, between the expected model data and the observed field data. Of the techniques discussed, this method requires the least multiplications per iteration (Bjorck, 1979); however, it often requires more iterations for moderate to severely ill-conditioned systems. Conjugate Gradient attempts arrive at a solution in fewer iterations by defining the vector, search direction and magnitude, needed to minimize the squared error. However, it's best suited for linear, positive definitive matrices. LSQR expands these methods using a least squares solution to the QR factorization of orthogonal matrices. Studies by Bjorck (1979) found that LSQR will arrive at more accurate solutions in fewer iterations for both well-conditioned and ill-conditioned systems as compared to OLS or Conjugate Gradient methods. However, for well-conditioned systems this effect is less pronounced. In

addition, even though fewer iterations are needed, more work is required per iteration for LSQR. For example, given a $m \times n$ matrix, LSQR expects 3m+5n steps per iteration; compared to 2m+3n steps for Conjugate Gradient. However, both are improvements over OLS with expects m^2n steps. Although, LSQR is the better general solution to the problem, the increased efficiency might not always justify the increased complexity for well-conditioned or small systems where Conjugate Gradient or OLS will prove more than adequate.

Chapter 5

FORWARD MODELING

Forward modeling can be used to illustrate the principles of tomography by the inversion of a known, parametrically defined data set (often referred to as a synthetic model in the literature) and by comparing the resulting tomogram to the original velocity model. As shown in Figure 5-1, three synthetic models with increasing levels of complexity are calculated from idealized components of the Time-Propagation (TP) mixing model for this thesis. Five raytracing techniques are analyzed: Geometric, Gaussian, Fast Marching Method, NORSAR Wavefront Construction, and Huygens' Waveray Tracing. First arrival travel times (FATT) are found for numerous pre-defined transmitter and receiver locations, which will be the inputs for the inverse problem. The inversion is then performed using Least Squares, Conjugate Gradient, and LSQR algorithms. A comparison of the computation work required and resulting error are provided.

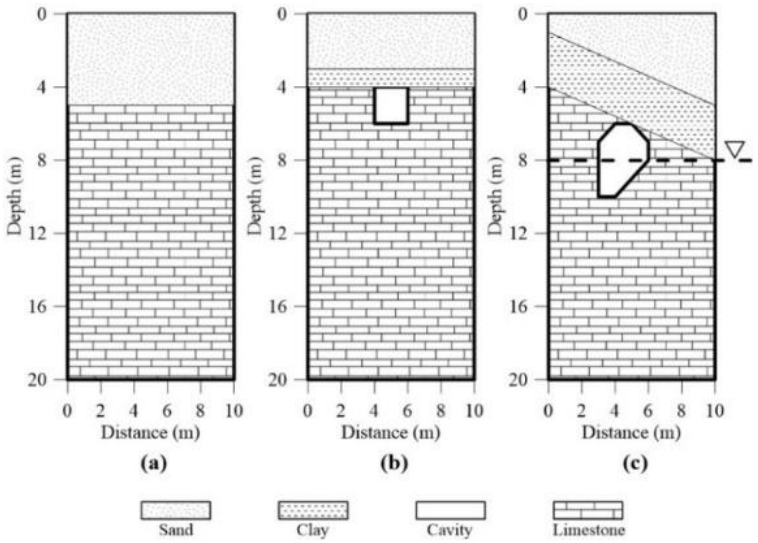

Figure 5-1, Synthetic models used in this study: (a) two-body permittivity model, (b) multi-body porosity model, and (c) complex saturation model

5.1. Material Properties and Synthetic Models

In its simplest form, the time-propagation (TP) mixing model must contain at least one parameter for material permittivity. Within geological materials there exists a range of relative permittivities for each material based on the natural variation of the formation (Table 5-1). In natural deposits, these materials are expected to have a considerable amount of overlap.

Table 5-1 Common relative permittivity values of materials in the synthetic models

Material	Relative Permittivity (ε_r)			Used in this thesis
	Annan 2009	Cassidy 2009	Daniels 2007	
Air	1	1	1	**1**
Water	80	78 - 88	80	**80**
Sand	3 - 5	3 - 6	4 - 6	**4**
Limestone	4 - 8	4 - 8	7	**7**
Clay	5 - 40	N/A	2 - 6	**6**

5.1.1 Two-body Permittivity Model

For this thesis, a common value was selected for each material type (notated in Table 5-1). Variations will be accounted for in later sections by including additional information into the model, such as porosity and saturation parameters. The first synthetic model, called the "two-body permittivity model", consists of two distinct segments of uniform material properties separated by a horizontal paraconformity. The uppermost 5 meters of the cross-section are clean sand with a constant relative bulk permittivity of 4. It overlays an idealized limestone formation that extends from 5 meters below ground surface to the bottom of the borehole. This lithified material is assumed to have a relative bulk permittivity of 7 (Figure 5-2).

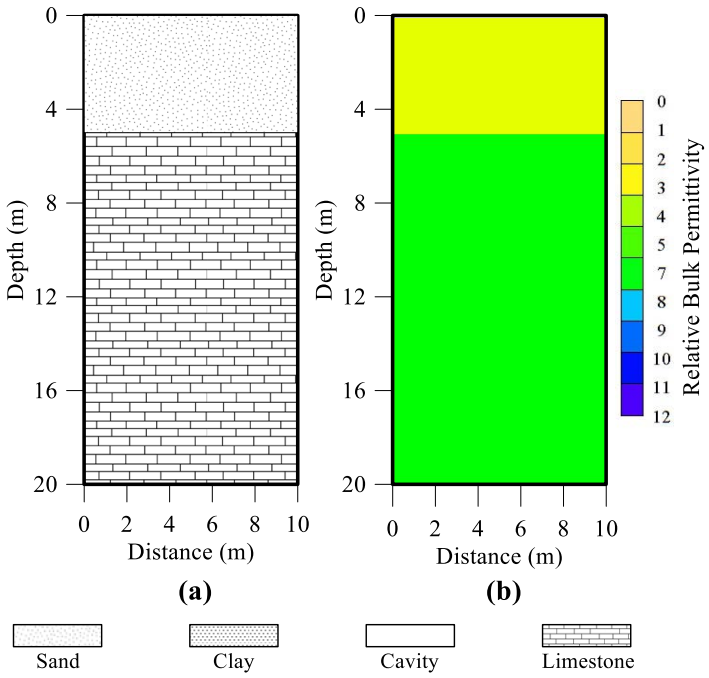

Figure 5-2, Bulk relative permittivity of the two-body permittivity model

The in-situ material variation is more accurately approximated by adding porosity assumptions to the permittivity model. This would be similar to a real cross-section of dry material above the water table. Since the formation is considered dry, the additional porosity information consists of air-filled pores entrained in the formation. The aggregated permittivity, called the bulk permittivity, can be calculated from the percentages of air and material using a matrix of the material's porosity valves (Eqn. 5-1). For example, given a clean sand with a relative permittivity of 4 at 30% porosity, the radar velocity should increase by 18% using the time-propagation mixing model. For the special condition of zero saturation, the TP mixing formula is given in Eqn. 5-1.

$$\varepsilon_B = \left[(1-\eta)\sqrt{\varepsilon_{matl}} + \eta\sqrt{\varepsilon_{air}}\,\right]^2 \qquad \textit{Eqn. 5 - 1}$$

5.1.2 Multi-Body Porosity Model

A second forward model is developed using permittivity and porosity material properties for each material type. In addition to the simple sand and limestone bedding of the previous model, the "multi-body porosity model" consists of a thin clay lens and a square void. The cross-section has 3 meters of sand overlaying 1 meter of clay, which sit atop limestone with a horizontal paraconformity. The limestone extends to the bottom of the borehole. An idealized 2 meter by 2 meter cavity is present 4 meters below the surface spanned by the clay layer and at the horizontal midpoint of the formation (Figure 5-3a). A constant relative bulk permittivity is assigned to each material. Common porosity ranges for clay and limestone were developed using USGS published values for material of Eocene age material (Manger, 1963). Porosity models are created for each material type as a function of depth. Based on Gluyas and Cade (1997), a porosity model for sand was created using Eqn. 5-2.

$$\eta = 0.40 \exp\left(\frac{-10^{-3} z}{0.24 + 5 \cdot 10^{-4} z}\right) \qquad \textit{Eqn. 5 - 2}$$

Where

η is the material porosity

z is the depth of the material in meters.

The porosity for sand varies exponentially from 40% to 37%, top to bottom of the cross-section, respectively. Models for clay and limestone are assumed to be linearly varying from 37% to 26% and 25% to 17%, respectively. The expected porosities were calculated for the approximate depths for the corresponding material types (Figure 5-3b). These values where then merged into a porosity as shown in Figure 5-3c.

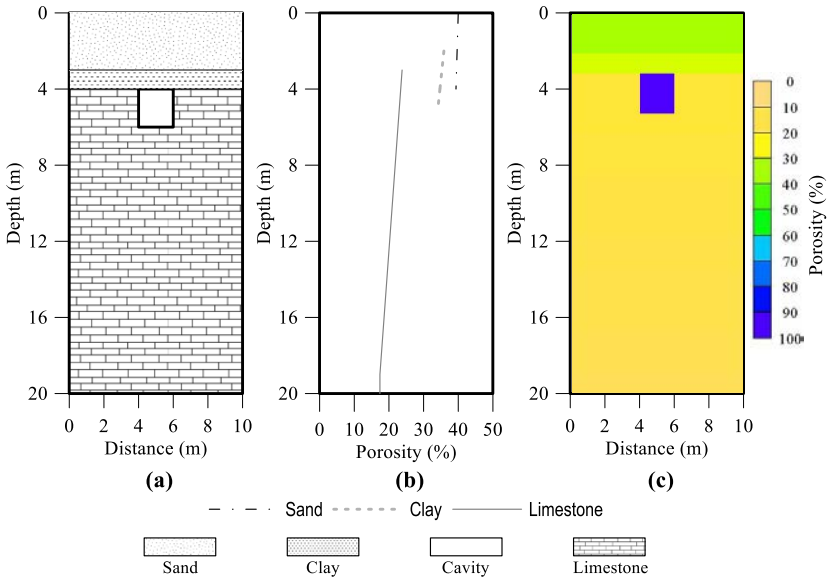

Figure 5-3, results of the porosity distribution analysis. (a) multi-body porosity mode, (b) variation of porosity with depth, and (c) forward model of derived porosity within the model.

Relative permittivity is then calculated, similar to the technique applied to the two-body permittivity model. The porosity model is incorporated into the permittivity model using the TP mixing model formula with the special condition of zero saturation (Eqn. 5-1) to determine the relative bulk permittivity of the cross-section (Figure 5-4b).

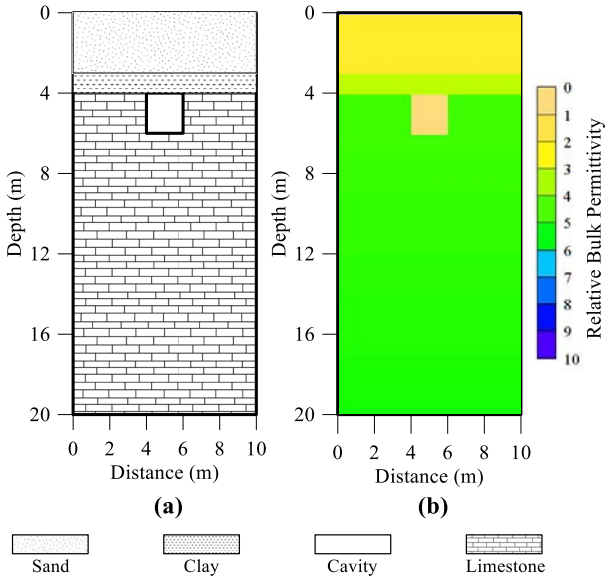

Figure 5-4, Results of the forward model for the multi-body porosity model

5.1.3 Complex Saturation Model

The final component of the TP mixing model is saturation. In the previous cross-section, air-filled voids were added to the model as porosity. By adding saturation, the possibility of at least partially water-filled voids is included. The bulk permittivity can be calculated from the relative permittivity, porosity, and saturation as shown in Eqn. 5-3.

$$\varepsilon_b = \left[(1-\eta)\sqrt{\varepsilon_{solid}} + \eta \cdot S\sqrt{\varepsilon_{water}} + \eta \cdot (1-S)\sqrt{\varepsilon_{air}}\right]^2 \qquad \textit{Eqn. 5 - 3}$$

Saturation is a measure of the amount of water present within the pores of a geological material. It ranges from 0%, no water in the pores, to 100%, all pores filled with water. Material below the water table is considered to be 100% saturated. The unsaturated soil above the water table is known as the vadose zone. Because of capillary rise of water into the soil matrix, this zone can be partially saturated. Since water has such a significant effect on the bulk permittivity, it is useful to model the water content within the vadose zone (Giroux and Gloaguen, 2011). In general, water moves from higher potential energy to lower potential energy along an energy gradient. Yet as grain-size becomes small, as seen in geological materials, a pressure potential is developed from capillary rise into the soil column and adsorption onto the soil grain. The combination of these phenomenon result in a negative pressure on the water column, known as matric suction potential. As gravitational potential energy increases with height above the water table, water flows towards the water table, the matric suction reduces the gravitational potential near the water surface. As the system approaches steady state conditions, negative pore water pressures will draw water into the soil matrix, creating partial saturation values. A Soil-Water Characteristic Curve (SWCC) describes the relationship between soil water content and matrix potential. Capillary rise is a function of surface tension and grain-size diameter; it can be directly related

to the material's grain size. In general, soils with higher clay content have higher water content. Conversely, coarse sandy soil with larger grain sizes will hold less water above the water table. This is described using the van Genuchten (1980) model for SWCC development (Eqn. 5-4).

$$S = [1 + (\alpha h)^n]^{-m} \qquad \textit{Eqn. 5 - 4}$$

The parameter α is a proxy for the air-entry pressure, or the minimum matric suction potential for air to recede into soil pores. The pore size distribution is related to the parameter n; the shape parameter of the SWCC is defined by the parameter m; and h is the distance from the water table. In the absence of detailed field data, the parameter m (Eqn. 5-5) is often simplified as a function of the n parameter (Genuchten, 1980).

$$m = 1 - 1/n \qquad \textit{Eqn. 5 - 5}$$

In this thesis, parameters for the SWCC model follow Meyer et al. (1997) analysis of the Natural Resource Conservation Services (NRCS) database summarizing over 15,000 soil specimens. Parameters for limestone follow experimental data collected by Likos et al. (2013).

Table 5-2, Soil-Water Characteristic (SWCC) Parameters used in this thesis

Parameter	Sand (Meyer et al., 1997)	Clay (Meyer et al., 1997)	Limestone (Likos et al., 2013)
α	1.50	0.10	0.51
n	2.68	1.13	2.60
m	0.627	0.115	0.615

Using the previously stated assumptions, the final TP mixing model can be constructed. The cross-section, called the "complex saturation model", consists of sand overlaying clay on a dipping limestone

formation approximately 18 degrees from horizontal. There is an oblong void from 6 meters below ground surface to 12 meters below ground surface that is 4 meters wide at its longest span. The water level is static at 8 meters below ground surface and bisects the partially water-filled void. The partially saturated vadose zone above the water table varies per the van Genuchten model using the material parameters from Table 5-2. From Figure 5-5b, it is shown that clay has very little reduction in water content at shallow depths. However, limestone and sand show a significant change in water content in terms of distance to the water table.

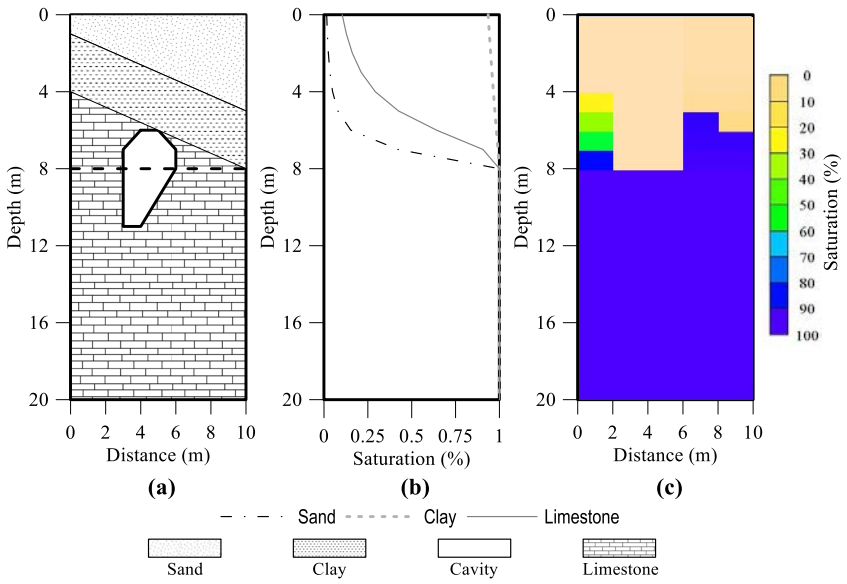

Figure 5-5, results of the saturation distribution analysis. (a) complex saturation model, (b) variation of saturation with depth, and (c) forward model of derived saturation within the model.

The bulk relative permittivity is then computed similar to previous models (Figure 5-6). The relative bulk permittivity constants for each material type are used. The porosity component varies by the same function as the previous model. The saturation component is then incorporated into the model using the full TP mixing model formula (Eqn. 5-3). Care is taken around the void, such that within the water table the permittivity matching that of freshwater is used and above the water table the permittivity matches air.

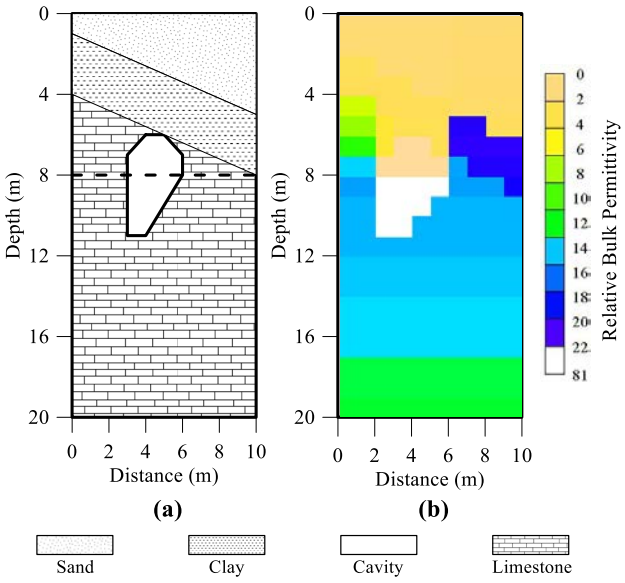

Figure 5-6, Results of the forward model for the complex saturation model

5.1.4 Material Classification

As shown, including porosity in the permittivity only model creates a more realistic cross-section; there is a decrease in bulk permittivity as the porosity increases. In dry geological materials, porosity can be thought of as adding air-filled voids into the geological matrix. Air has a relative bulk permittivity of 1, lower than most geological materials. Therefore, by including air into the bulk material properties, the relative bulk permittivity is reduced. Similarly, water has a relative bulk permittivity much higher than most geological materials (approximately 80). Compared to common materials, such as sand, clay, and limestone, the relative magnitude of the permittivity of water is several times higher than that of air. Therefore, when the voids from the inclusion of porosity are filled with water, the relative bulk permittivity is significantly increased. The magnitude of this shift creates overlap in the bulk permittivity of different materials (Table 5-3).

Table 5-3, Common values of relative bulk permittivity (Cassidy, 2009).

	Relative Permittivity (ε_r)	
Material	**Dry**	**Moist**
Limestone	4 - 8	6 - 15
Sand	3 - 6	10 - 30
Clay	3 - 6	2 - 20

However, if the degree of saturation is known (or if it can be estimated), defining the presence of water, because of the difference in magnitude between and air-filled void and a water-filled void, increases the signal-to-noise ratio in the bulk permittivity model. To expand on this idea, Figure 5-7 shows the occurrence of the bulk permittivity for the complex saturation model. The distinction between unconsolidated and consolidated materials is obvious (Figure 5-7b), but within each of these groups it's difficult to distinguish specific materials. If the histogram is split into two figures separated by the permittivity value of, say, 10 as shown in Figure 5-7a and 5-7d, we see that sand and limestone have a very strong signal with a wide bandwidth. Due to its low hydraulic conductivity, clay is the material with the greatest range. Occurring in both the lower permittivity range (Figure 5-7c) and the upper permittivity range (Figure 5-7d), clayey materials have the greatest range in the presence of water and are primary contributor to the overlap in GPR classification. By using a three component model, like the TP mixing model, this overlap can be used to extract more information from the model. For example, in Figure 5-7c (dry histogram) the permittivity ranges from 0 to 7. However, using Figure 5-7d (wet histogram) the permittivity ranges from 0 to 26. If it is assumed that a relatively bulk permittivity is constant for a specific material type and a known saturation, the porosity is much easier to distinguish by removing saturation from the model (Figure 5-7 (a)).

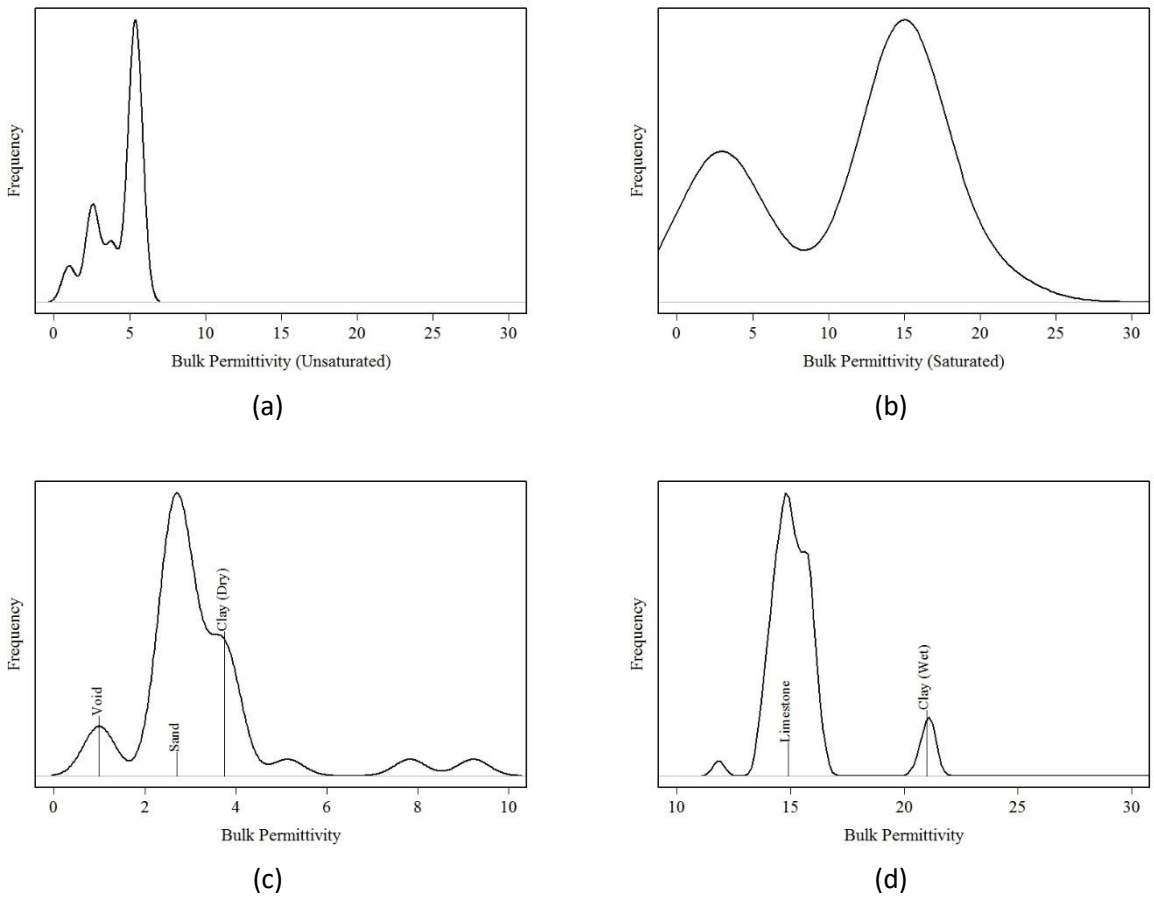

Figure 5-7, Density plot of relative permittivity of different material types for the Complex Saturation Model. (a) The unsaturation portion of the cross-section, (b) the saturation portion of the cross-section, (c) lower permittivity range of saturated material, and the (d) upper permittivity range of saturated material.

5.2. Raytracing

Five raytracing techniques were analyzed for each synthetic model: Geometric, Gaussian, Fast Marching Method, NORSAR wavefront construction, and Huygens' waveray tracing. Even though each technique has a similar goal and often has a similar first arrival travel time, there can be significant deviations along the wavefronts. Care should be taken when selecting a raytracing technique. Since raypaths are used in the inversion process, differences could result in vastly different inverse model results.

5.2.1 Two-Body Permittivity Model Raytracing

The two-body permittivity model has a consistent cross-section with a single interface between material types. Because of the simplicity of this model, it is expected that there should be minimal variation between raytracing techniques (Figure 5-8).

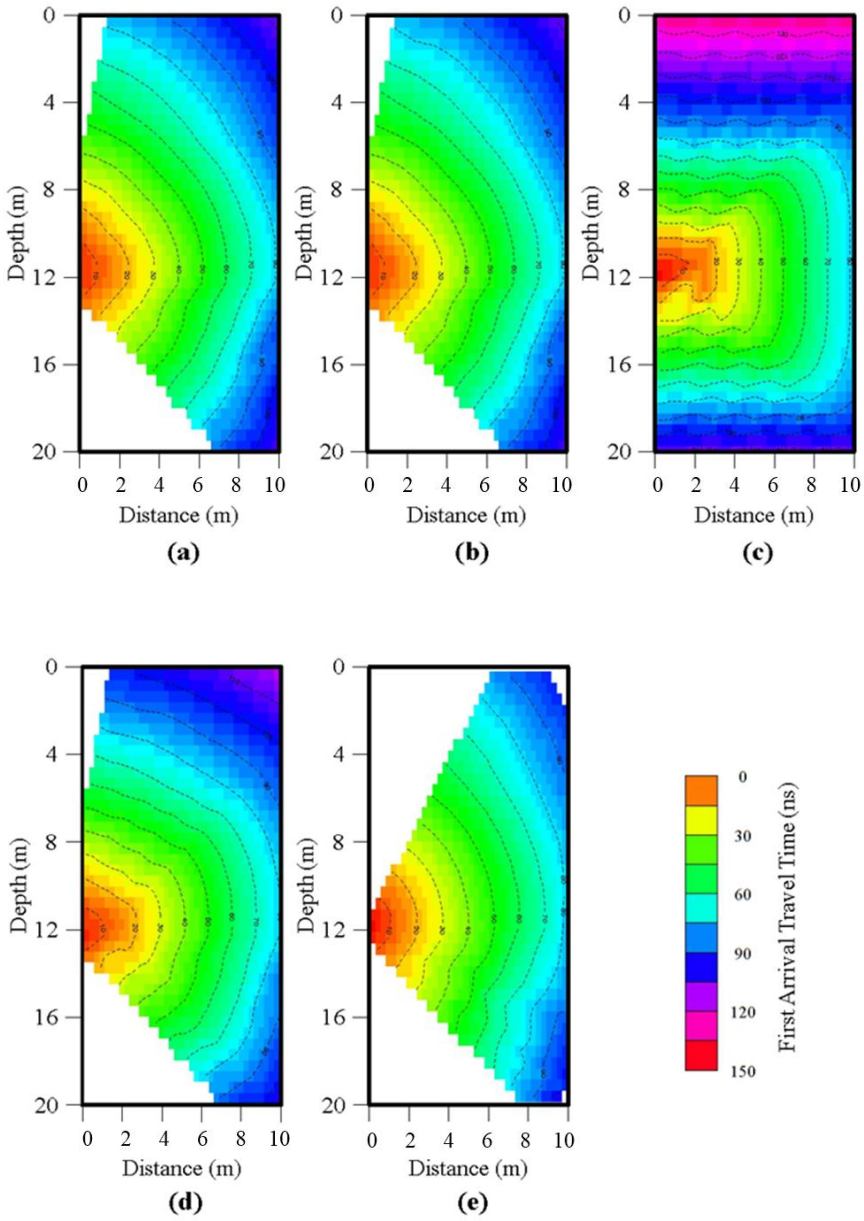

Figure 5-8, First arrival travel time contours of the Two-Body Permittivity Model from a transmission depth of 12 meters below land surface. (a) Geometric Raytracing, (b) Gaussian Raytracing, (c) Fast Marching Method, (d) NORSAR Wavefront Construction, and (e) Huygen' Waveray Tracing.

Both subtle and obvious differences are found. To illustrate this point, wavefronts are found for each technique from a single transmitter location 12 meters below ground surface. The models are similar with the exception of the Fast Marching Method (FMM). In general, a radiating quasi-circular wavefront propagation is observed. However, Figure 5-8c shows wavefronts in a rounded rectangular shape. The limitations of taking the first-order approximation of a Cartesian grid, tend to under-sample wavefronts near the source where a larger curvature is expected. This error continues throughout the formation. While the FMM is very stable and efficient, it should not be used on simple models with raypaths following spherical orthogonal systems, or wavefronts (Alkhalifah and Fomal, 2001).

Despite the differences in wavefront construction, the first arrival travel times as observed in the receiving borehole are similar throughout most of the borehole. The least variability is at the location horizontal to the transmitter location (12 meters below ground surface). As the shot angle increases the models diverge. As shown in Figure 5-9, the Geometric Raytracing and Gaussian Raytracing techniques are practically identical, which is expected because of the Gaussian averaging would provide little benefit in consistent material. Below the transmitter location, the FATTs for NORSAR Waveray Tracing and Huygens' Wavefront Tracing are similar and then diverge above the horizontal. The FMM differs at every location off the horizontal.

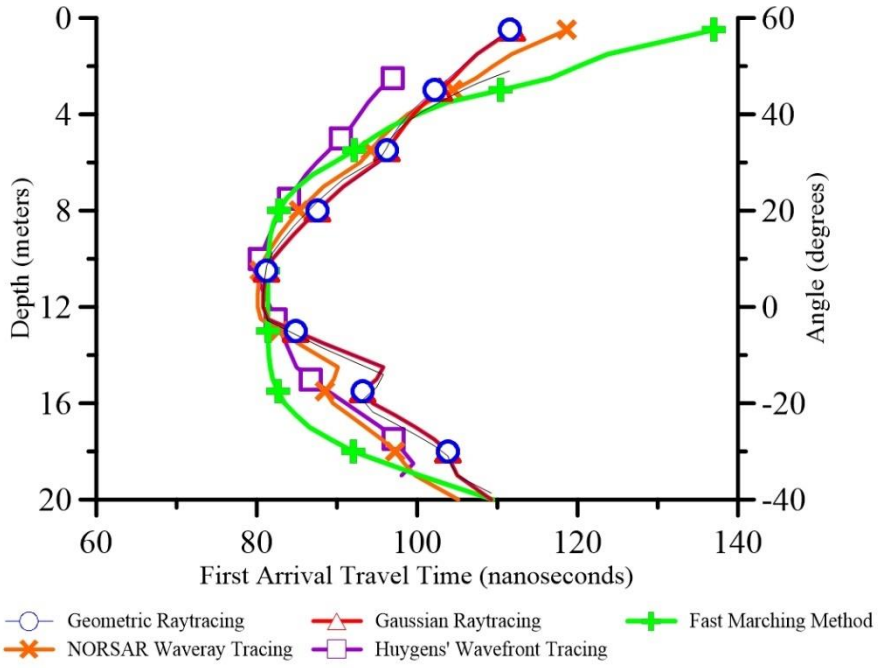

Figure 5-9, First arrival travel time for the two-body permittivity model at several receiver locations from a single transmitter location 12 meters below land surface

5.2.2 Multi-Body Porosity Model Raytracing

The multi-body porosity model has similar limitations. Even though this model is more complex than the previous model, the general shape of the wavefronts are similar. The majority of the techniques produce a quasi-circular propagation with the exception of the Cartesian FMM. The most significant variation follows the 2 meter by 2 meter void in the formation, located 4 meters below ground surface. All five of the models show a change in gradient following this anomaly. The Geometric Raytracing technique, Figure 5-10a, shows the largest change with of almost 5 nanoseconds from an estimated uniform contour. Figure 5-10b and 5-10d, show a similar, thought less drastic deviation. The Huygens' Wavefront Tracing, Figure 5-10e, shows a change as severe as Geometric Raytracing except with a smoother approximation of adjacent cells. Even the FMM (Figure 5-10c) shows a change, however it's plagued by the same approximation errors as the previous model.

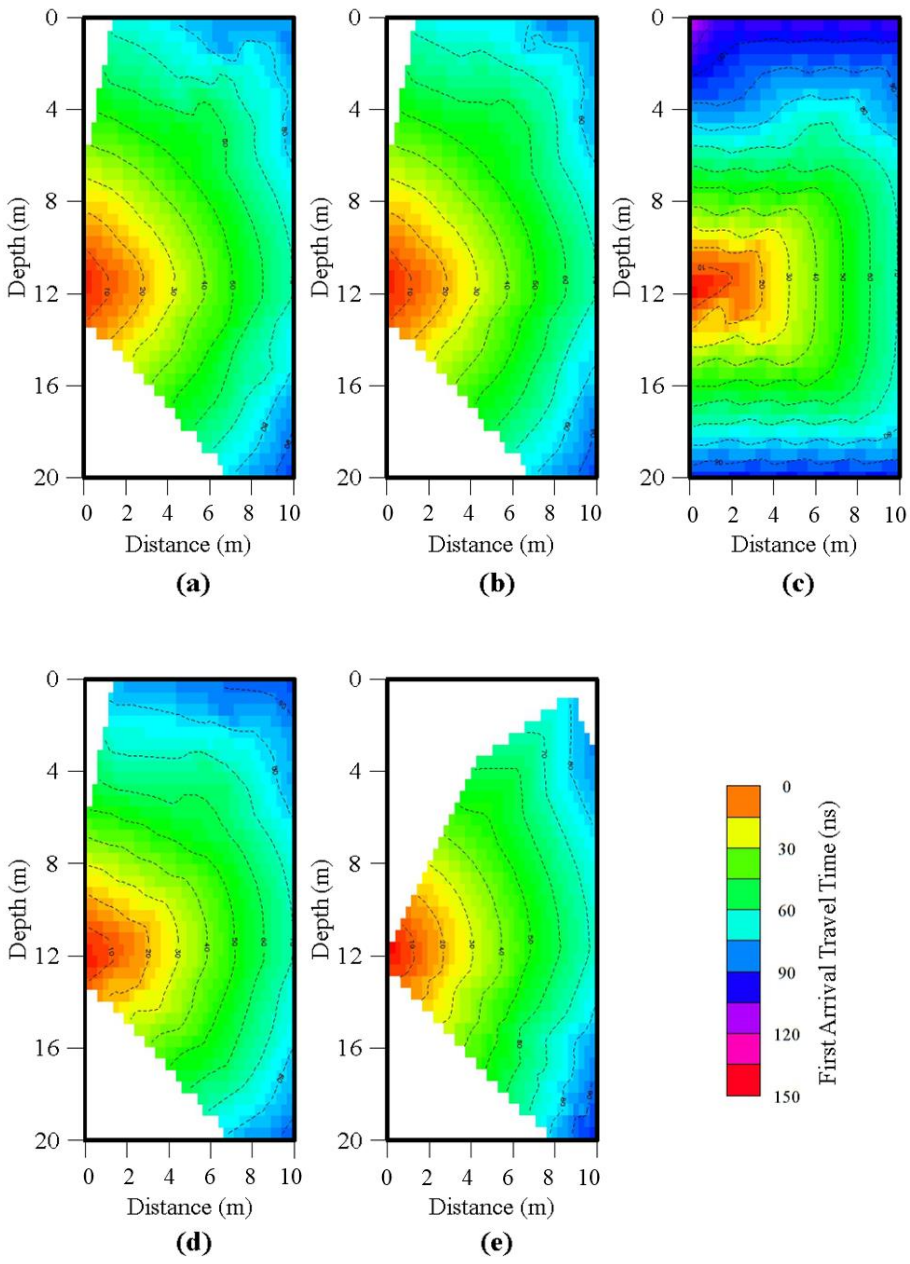

Figure 5-10, First arrival travel time contours of the Multi-Body Porosity Model from a transmission depth of 12 meters below land surface. (a) Geometric Raytracing, (b) Gaussian Raytracing, (c) Fast Marching Method, (d) NORSAR Wavefront Construction, and (e) Huygens' Waveray Tracing.

Other than the FMM, there is little variation between the First Arrival Travel Times at the receiving borehole (Figure 5-11). The Geometric Raytracing, Gaussian Raytracing, and Huygens' Wavefront Tracing methods are closely related throughout the graph. The travel time above 6 meters below grade are affected by the air-filled void. Since air has a lower permittivity than any other geological material, the

radar velocities are increased relative to the surrounding media; resulting in a decrease in FATT. The NORSAR Waveray Tracing technique is less sensitive to this change, this method is recommended it when the model contains a region of higher velocity (such as an air-filled void) over a region of lower uniform velocity (Tweedon, 2008))

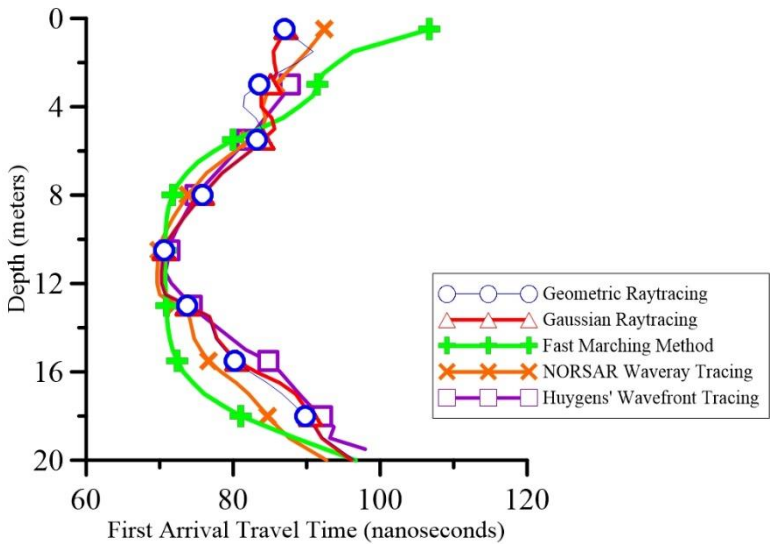

Figure 5-11, First arrival travel time for the multi-body porosity model at several receiver locations from a single transmitter location 12 meters below land surface

5.2.3 Complex Saturation Model

The Complex Saturation Model has wavefront formations similar to the previous model, with the exception that the void is much larger and partially water filled. Since water has a much higher permittivity than any other geological material, critically refracted rays are expected in the area. While similar below the void, each of the five models has distinct variations due these critical refractions. This area is often referred to as the shadow zone. Within this complex cross-section, the discrepancy between the FMM and the other techniques is minimized. Except for the triangular segment from 12 meters below ground surface at the transmitting borehole to the point 7 meters horizontal at the bottom of the borehole, the FMM roughly matches the other techniques below the horizontal. This is in part due to the stability of the method, which allows the full cross-section to be computed. Since these values do not reach the receiving borehole they could be excluded. However, in the shadow zone the FMM has the greatest difference compared to the other methods. In part, this is due to the saturated clays within this

zone. Since FMM does not rely on raytracing, it is more stable in areas of discontinuities and high variations in velocity (Sethian, 1998). In the area, above the shadow zone the Gaussian Raytracing technique, Figure 5-12b, closely resembles the FMM as shown in Figure 5-12c. Since the Gaussian method averages the permittivities adjacent to the raypath, it is more stable in critically refracted zones compared to the Geometric Raytracing technique, Figure 5-12a. The NORSAR Waveray tracing, Figure 5-12d, is roughly similar to the Geometric Raytracing technique above the shadow zone, but within the shadow zone FATTs are lower than the other methods. While the Huygens' Wavefront Tracing technique shown in Figure 5-12e generally provided smoother contours in previous methods, it appears to bend around the shadow zone.

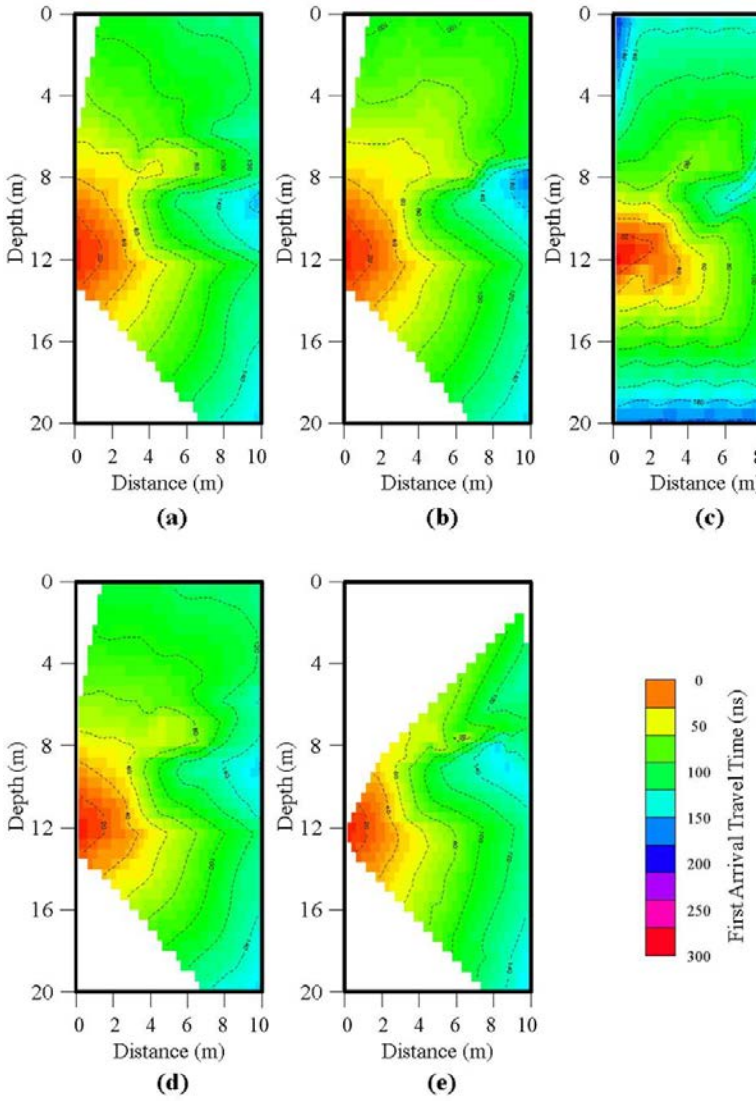

Figure 5-12, First arrival travel time contours of the Complex Saturation Model from a transmission depth of 12 meters below land surface. (a) Geometric Raytracing, (b) Gaussian Raytracing, (c) Fast Marching Method, (d) NORSAR Wavefront Construction, and (e) Huygens' Waveray Tracing.

As shown in Figure 5-13, the FATT below the void is similar for every technique. However, within the shadow zone there is significant discrepancy between methods, roughly 70% deviation. If used for inversion, severe errors would be expected. Above the void, with the exception of the Gaussian Raytracing technique, the methods converge again. Within the shadow zone the travel times are generally longer below the water table and shorter above the water table. There is an inverse relationship between permittivity and radar velocity. Therefore, the high permittivity of water is expected to cause lower radar velocities and longer travel times. The similarities between first arrivals above the shadow shows that despite the instabilities within the void, the disturbance is limited.

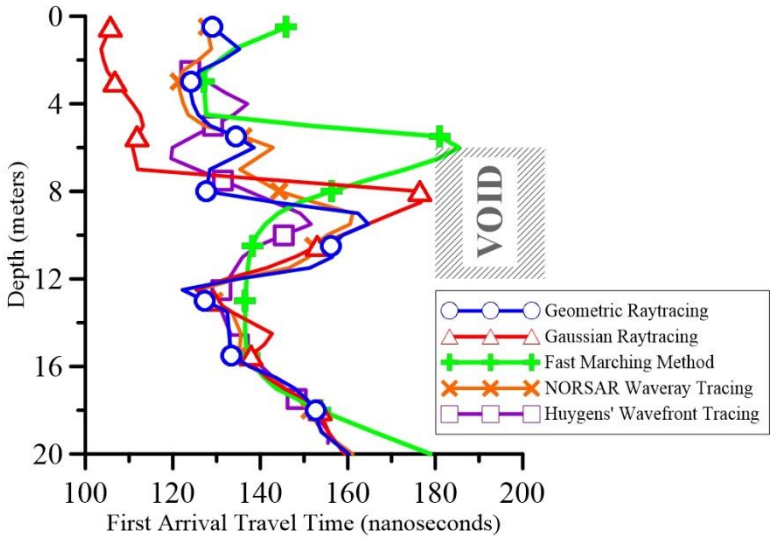

Figure 5-13, First arrival travel time for the complex saturation model at several receiver locations from a single transmitter location 12 meters below land surface

5.3 Inversion Schemes

Considerable improvements in terms of inversion speed and memory usage can be realized by using more complex inversion algorithms, such as Conjugate Gradient or LSQR, as opposed to Ordinary Least Squares (Paige and Saunders, 1982). For a small cross-section, such as those found in GPR tomography, the cost of implementation may not always justify the improvement of efficiency. Each of

the three forward models consists of large sparse matrices, ranging from moderately to severely ill-conditioned systems. The Two-Body Permittivity model has the lowest condition number ($\log_{10}K$ of 3.21), followed by the Multi-Body Porosity Model ($\log_{10}K$ of 5.15), and Complex Saturation model has the highest condition number ($\log_{10}K$ of 7.76). Table 5-4 shows the number of iterations per inversion from applying each algorithm to each of the forward models.

Table 5-4, Comparison iterations per inversion using each of the inversion algorithms for each model

Algorithm	Two-Body Permittivity	Multi-Body Porosity	Complex Saturation
Ordinary Least Squares	31	33	80
Conjugate Gradient	51	72	92
LSQR	24	26	67

In terms of number of iterations to perform the inversion, there is a notable difference between each inversion technique. For the moderately ill-conditioned Two-Body Permittivity model the Conjugate Gradient (CG) method requires twice as many iterations as the LSQR method. The Ordinary Least Squares (OLS) method only requires slightly more iterations than the LSQR method. There are similar results for the Multi-Body Porosity Model. LSQR and OLS are similar, while CG is three times as many iterations as LSQR. However, the effects of this trend do not continue into the severely ill-conditioned Complex Saturation model results. In this final model, the difference between the number of iterations required for OLS and CG is much smaller. LSQR is still requires less iterations than the other two methods, but not by much (16% less than OLS). The true effect on computation speed is found by incorporating the number of multiplications per iterations. Based on work by Paige and Saunders (1982), for the previously defined forward models, Conjugate Gradient is expected to require the least work per iteration (1,800 multiplications per iteration). Ordinary Least Squares requires the most work (2,700 multiplications per iteration), followed closely by LSQR (2,400 multiplications per iteration).

As shown in Table 5-5, every instance the LSQR algorithm requires less total work, measured in terms of multiplications required for inversion, than the other methods used in this analysis. For the moderately ill-conditioned matrices, OLS performs better the CG. However, for severely ill-conditioned systems there is a noticeable benefit to using either the CG or LSQR algorithms over the OLS. For this study, even though computational improvements can be realized by using more sophisticated inversion algorithms; marginal practical improvements are found. For example, on a consumer-grade computer with a 3.0 GHz processor there is little difference in computation time between 216,000 multiplications for OLS and 160,800 multiplications for LSQR.

Table 5-5, Comparison multiplications per inversion (in thousands) using each of the inversion algorithms for each model

Algorithm	Two-Body Permittivity	Multi-Body Porosity	Complex Saturation
Ordinary Least Squares	83.7	89.1	216.0
Conjugate Gradient	91.8	129.6	165.6
LSQR	57.6	62.4	160.8

5.3.1 Model Accuracy

Forward modeling is a tool to illustrate the accuracy and application for each pair of raytracing and inversion methods. From a known velocity model, the error can be directly calculated. Each of the three synthetic models: Two-body Permittivity, Multi-Body Porosity, and Complex Saturation have unique features that are better suited for certain techniques. A common method to measure error is the root mean squared error (RMSE), where the difference between the calculated value and the modeled value is squared for each cell. Then the square-root of the averaged squared difference for the entire matrix is calculated. It is similar to the L-2 norm method used in OLS inversion. Calculated values further from the actual value are given a higher weight than values closer to the actual value. Averaging the terms put the squared deviation into a magnitude representative of the dataset, as opposed to summing the values as

used in the common sum of squared error (SSE) measurement that often results in a value several orders of magnitude higher than the mean squared error. The average squared error is then transformed back into the units of the original problem by taking the square-root.

From Table 5-6, regardless of the model and raytracing technique, the inversion algorithms follow a consistent pattern. For any raytracing method, LSQR has a lower RMSE than Conjugate Gradient, which has a lower RMSE than Ordinary Least Squares. This is an interesting result. At least for the models in this thesis, the LSQR inversion method is more accurate that the other methods regardless of the model or raytracing method used.

Table 5-6, Root Mean Squared Error (RMSE) for each of the three models: Two-Body Permittivity, Multi-Body Porosity, and Complex Saturation using each of the five raytracing techniques: Geometric, Gaussian, Fast Marching Method, NORSAR Wavefront Construction, and Huygens' Waveray Tracing for each of the three inversion algorithms: Ordinary Least Squares, Conjugate Gradient, and LSQR.

	Two-Body Permittivity			**Multi-Body Porosity**			**Complex Saturation**		
Raytracing Technique	**OLS**	**CG**	**LSQR**	**OLS**	**CG**	**LSQR**	**OLS**	**CG**	**LSQR**
Geometric Raytracing	0.012	0.011	0.009	0.025	0.020	0.016	0.047	0.038	0.038
Gaussian Raytracing	0.013	0.011	0.010	0.024	0.021	0.018	0.039	0.035	0.028
Fast Marching Method	0.017	0.015	0.013	0.025	0.022	0.020	0.039	0.033	0.029
NORSAR Wavefront	0.009	0.008	0.007	0.024	0.020	0.016	0.042	0.039	0.029
Huygens' Waveray	0.009	0.008	0.007	0.022	0.018	0.018	0.041	0.034	0.031

Raytracing methods show significant variation depending on the application. For example, Geometric Raytracing performs well for the Two-Body Permittivity and Multi-Body Porosity model (0.009 and 0.016 respectively using LSQR). It has one of the lowest RMSE for each. However, for the Complex Saturation model Geometric raytracing has a much higher RMSE than the others. This is likely attributed to critical refractions about the regions of contrasting velocities, such as the air-water interface within the partially-filled void or the shadow zone discussed in the raytracing section of this chapter. Conversely, Fast Marching Method (FMM) has the highest RMSE for the first two models (0.013 and 0.020 respectively

using LSQR) and one of the lowest RMSE for the Complex Saturation model. Confirming that even though FMM may not be suited for simple models, it tends to perform well in models with adjacent contrasting velocity zones and complex material placement. The other wavefront method, NORSAR wavefront construction, generally performs better than the FMM, roughly 30% better on the Two-Body Permittivity and Multi-Body Porosity models. But, the two methods are almost identical with the Complex Saturation model. In addition, compared with NORSAR Wavefront method, Huygens' waveray tracing has similar performance (average RMSE is within 3% of each other). Both methods perform well across the full range of simple to complex models. Unfortunately, wavefront construction methods are more common in academic research than in commercial software packages (Audebert et al., 2001). So, while it may be the best method to use, practical implementation maybe limited by the industry standards. Given this observation, the best practice found by this thesis is to use Gaussian Raytracing with LSQR inversion. Using the LSQR inversion technique, Gaussian Raytracing outperforms the other methods, including NORSAR wavefront construction and Huygens' waveray tracing, in the complex model and produces results at least as good as the other raytracing methods on the simpler models. It's common to most tomography software packages and produces reliable results regardless of the complexity of the geologic bedding.

5.4 Chapter Summary

This chapter applies the techniques described in the previous chapters, such as the electromagnetic properties of materials (Chapter 2), raytracing schemes (Chapter 3), and inversion algorithms (Chapter 4), to three models of varying properties to compare the benefits and limitations GPR tomography within common geological features. The first model describes one of the simplest models that could occur in the field, a homogenous lithology with horizontal layering of two distinct materials. This was called the Two-Body Permittivity model. In general, any combination of raytracing and inversion techniques yielded relatively lower RMSE values for this model. The second model builds on the first by

introducing porosity variation as a function of depth. An air-filled void is also included to induce critical refraction from the raytracing algorithms. This was called the Multi-Body Porosity model. The RMSE results for this model are similar across the techniques with the wavefront methods NORSAR wavefront construciton and Huygens' waveray tracing, generally performing better with the raytracing techniques: Geometric and Gaussian. However, improvements from the LSQR inversion algorithm over Ordinary Least Squares and Conjugate Gradient, reduce the difference between raytracing techniques to a negligible amount. The final model includes complex lithologies of several different material types on a dipped bedding plane with a massive partially water-filled void. The model is designed to disrupt the raytracing schemes by providing contrasting velocity zones and non-horizontal paraconformities. This was called the Complex Saturation model. For this method, wavefront techniques perform much better than raytracing techniques with the except of Gaussian raytracing, which had the lowest RMSE using the LSQR inversion algorithm. Based on this thesis, it's recommended that Gaussian raytracing with LSQR inversion algorithms should be used for field work in geological settings similar to the forward models previously described.

Chapter 6

INVERSE MODELING

In the forward model, raytracing and inversion techniques were applied to ideal datasets. Since the dataset is known model errors can be directly correlated. Inverse modeling involves collecting field data for the boundary conditions, then by applying raytracing and inversion techniques a dataset is developed. It is difficult to calculate model error with reasonable certainty (Lehikoinen et al., 2007), therefore engineers often rely on site characterizations, driller's logs, or other geophysical techniques to resolve uncertainties.

6.1 Data Collection

The data collection procedure for cross-borehole GPR tomography often begins with at least two PVC cased small-diameter boreholes. The cross-sectional area between and perpendicular to the boreholes is the material to be classified. For convenience, each borehole should be named and geo-located. Site geometry is an important parameter in determining radar velocity. The depth of each borehole, the separation between boreholes, any topographic changes, and the height of the top of casing above ground level should be recorded. Since water has a significant effect on relative bulk permittivity it is important to measure the water level at the beginning and end of the data collection.

Improper field techniques are the greatest source of error in GPR tomography (Gloaguen et al., 2007). It is important to develop a method to maintain accurate and consistent antenna placement. It can be as simple as marks on the antenna cable or as sophisticated as a digital gauge on a motor-operated winch. Regardless of method, a plan should be determined prior to any field work. For example, due to signal attenuation it is rarely practical to collect incremental data from every step

between the top and the bottom of each borehole (Irving et al., 2007). A maximum vertical distance should be estimated using assumed material properties. Based on these limitations the starting and ending depths of each gather may vary compared to sequential gathers from the top to the bottom of each borehole. It is good practice to develop a table correlating trace number to transmitter and receiver depths. Often this information is needed to correct input data in the tomography model. Based on information from this table, an operator will hold (or clamp) the transmitting antenna at a fixed location while the receiving antenna is lowered to various locations. At the end of the gather—when the final receiver location has been logged—the transmitter is moved to the next location and the receiver is again varied. This is repeated for the entire depth of the transmitter borehole.

6.2 Filters

All GPR data requires at least some form of basic processing (Annan, 2009). The equipment used to collect the data and the environmental conditions during the data collection can affect the calibration of the trace. In addition to any post-collection corrections, most GPR units perform minimal field correction to improve the visualization of the data to confirm field collection techniques on-site. Common filters are desaturation and gain filters.

Desaturation, often called declipping, reduces the peak amplitude of high-amplitude waves. These so called saturated waves, can distort secondary waves along the trace by artificially raising the relative amplitude of the entire time window. A negative gain is applied to reduce the wavelet's peak value and the wavefront is artificially recreated using spline interpolation.

Alternatively, weak signals are improved by applying gain to the waveform. There are two general gain functions that are used at this step: constant gain functions or Automatic Gain Corrections (AGC). Constant gain functions multiply the signal by a function. Common functions are a constant value, linear function, or an exponential function. A second method is to strategically adjust the gain functions

throughout the trace. Very small time windows (roughly 3% of the trace) are identified. The signal within that window is then scaled by a function of the ratio between the maximum amplitude of the trace and the mean amplitude of the time window (Annan, 2009).

After the data has been collected some basic processing is required to calibrate the trace. Thermal drift, variations in antenna construction, differences in cable length, and electronic instability can all contribute to discrepancies between the signal transmission and receiving times (Annan, 2009). To adjust for these factors a time-zero correction is required based on the straight-line travel time of a GPR pulse in air at a known distance, often call an "air shot". The air shot is used to find the absolute time zero and the entire trace is shifted to start at this time.

A signal offset and trend can be added to the trace though DC Bias, interference from early air-to-ground arrivals, or inductive coupling effects from the antenna. A common filter to resolve this issue is dewow. The first step is to reduce the mean amplitude of the signal to zero. This removes DC Bias and can improve the selection of first arrival travel times by allowing for positive-negative color coding. The next step is to correct for any signal drift, or wow, caused by low-frequency distortion (Daniels, 2007).

Basic filtering is required to put the data into an intelligible form. Several more advanced techniques can be used. However, it is important to maintain the integrity of the raw data and avoid over-enhancing the noise to create false signals. There are two types of filters applied after basic processing: temporal and spatial. Often the two can be combined into a single 2-D filter (Annan, 2009).

Temporal filters are used to reduce human-induced noise from the signal. They are applied to the time-frequency domain of a single trace. For example, high-frequency noise from radio signal can be removed by knowing the maximum possible frequency from the GPR unit and only allowing signals below this frequency (low-pass filter). Inversely, low-frequency signal drift and induced noise can be removed by knowing the minimum possible frequency from the GPR unit and only allowing signals above this

frequency (high-pass filter). Often the two filters are applied in unison to create a band-pass filter. Band-pass filters only record frequencies within a defined range. The simplest function is a notch filter, which can be represented as a vertical cut-off at each end of the passing spectrum. More advanced filters, such as the Butterworth filter, apply a uniform region for notch filter-type bypass and then gradually slope toward low- and high-pass cutoffs (Annan, 2009).

Spatial filters do not operate on a single trace like temporal filters; but along the time-axes of several traces. This technique is used to remove white noise from the trace, which is frequency-independent and cannot be removed in the frequency-domain. A common background removal technique is to take the mean of a group of similar traces and subtract the composite value from each trace. Since white noise has a mean of zero a DC Bias-type shift is not expected (Daniels 2007).

Gain is often applied again after filtering to improve the visual form of the trace. It is important to note that type of gain can affect the relative amplitudes and phase relationship of the trace (Annan 2009). Therefore, it's best practice to apply advanced gain filters after filtering. In addition to the previous mentioned functions, an energy decay or Spreading and Exponential Correction (SEC) gain filter can be used to adjust the gain in proportion to the loss of signal with time. It consists of two components. The first is an approximately $1/r^2$ function to correct the signal strength for loss to the geometrical spreading of the waveform. The second component is an exponential function designed to boost energy loss due to material attenuation.

6.3 First Arrival Travel Time Selection

After applying at least basic processing (absolute time zero correction is not optional), the onset of signal must be identified for each trace. The temporal location of the leading-edge of the recorded wavelet is called the First Arrival Travel Time (FATT). It is the time needed for the signal to travel between boreholes as measured from the creation of the GPR wave by the transmitting antenna to the initial

voltage change recorded by the receiving antenna. The first step is to combine the hundreds of individual traces into a single file. Then for each trace the leading front of the wavelet is notated. This is often an automated procedure; however, the human eye can be a better judge of ambiguity than software routines. For traces with low signal-to-noise ratios it is common to select an arbitrarily long travel time that can be filtered out later. The FATT for each trace is exported to tabular form. The horizontal and vertical location for each transmitter and receiver position for each trace should be verified and corrected as needed.

6.4 Field Testing

From the FATT boundary conditions, a tomogram is created by first raytracing an arbitrary velocity model and inverting the model based on the raypaths. An improved model results and the process is repeated until a minimum residual is obtained. For the initial velocity model, only the horizontal traces were used. Radar velocity is assigned based on the straight-ray travel time. The media along the path is assumed to have the same velocity as the neighboring cells on the same horizon. This is known as a Zero-Offset Profile (ZOP). Since the shot is at an incident angle of zero, the ray does not bend at the interface of different material radar velocity. Thus, it can be a useful tool to identify errors in the raytracing.

6.5 Geological Setting

The GPR cross-borehole testing was conducted at the UNF-UF-FDOT Geophysical test site, a four-acre dry retention stormwater pond in Newberry, Florida, roughly 15 miles west of Gainesville within Alachua County. The general stratigraphy is consistent with depositions found in historically marine environments and is common to the surrounding area. The site is distinguished by karst features overlaid by sand and clay. Specifically, regional subsurface material consists of undifferentiated siliclastic marine sediment of late Miocene to Plio-Pliestocene sands and terrace deposits that overlay the Hawthorne Group, which lays unconformably atop Ocala Limestone (Campbell and Scott, 1991).

Marine sediment blankets most of Alachua County at variable depth ranging from less than one meter to greater than six meters thick. The material is predominantly quartz sand ranging from fine to very coarse with some intermixed clays (Campbell and Scott, 1991). The Micocene to early Plio-Pliestocene Hawthorne Group is a complex interbedded group of intermixed carbonates and siliclastic facies. The compositions are highly-variable; including percentages of quartz sand, silt, clay, phosphate grains, and carbonate that are inconsistent horizontally and vertically within the cross-section (Scott, 2001). The Eocene aged upper Ocala Limestone is composed of white-colored, fossilferous packstone to grainstone ranging from partially to well-indurated and differs slightly from the partially dolomitized lower Ocala Limestone and older Avon Park Formation (Campbell and Scott, 1991). Significant dissolution has been observed in the formation at a rate of approximately 1.5 inches per 1,000 years due to natural weathering. From the development of secondary porosity, the rock has become highly-permeable with a porosity range of 20% to 55% (Brooks, 1967). Within the test site, the thickness of unconsolidated marine sediment and Hawthorne Group materials from 0 meters at Limestone outcrops to 7.5 meters thick.

6.6 Field Procedure

The test site has five 100 millimeter diameter PVC-cased boreholes grouted in place using a low-strength slurry to match the existing material properties. During casing installation, stratigraphy was determined by driller logs and cuttings from a tricone bit. The boreholes are roughly 18 meters deep and arranged in a "cross" orientation with four outer boreholes along the cardinal axes with a single inner borehole centrally located. The outer boreholes are approximately 3 meters from the inner borehole. The northern most borehole is named borehole "A", with the naming scheme continuing in alphabetical order in a sequential clockwise pattern. The center borehole is named "X". The water table during the test was at 6 meters (19.6 feet) below ground surface. To begin data collection, the transmitter and receiver were lowered to an initial depth of 1.83 meters (6 feet) below ground surface. Next, the receiver

was independently lowered at uniform increments of 0.61 meters (2 feet) while the transmitter remained stationary. A trace was recorded for each location. The collection of traces from a single transmitter location is known as a gather. The transmitter was then repositioned 0.61 meters (2 feet) lower and the gather process repeated. An average of 18 traces were recorded in each gather. A total of 489 traces were recorded for each pair of boreholes. Between each set of boreholes the antennas were brought to the surface and a calibration for absolute time-zero was performed. The data was collected from a 100MHz borehole antenna system from Sensors & Software using an antenna that was 3 centimeters in diameter and 1.44 meters in length. Each trace was stacked 16 times and an AGC gain filter was applied to improve field resolution. Desaturation was not applied.

6.7 Data Processing

After the field data was collected, several commercial software packages were used to interpret the data. The first step was to load the traces into EKKO_View Deluxe (Version 1 Release 3) to merge the traces from each set of boreholes into a single file. Absolute time-zero correction was applied and the time window was clipped to the maximum theoretical travel time (usually around 250 ns). The data was loaded into TomTime (GeoTom, LLC) and filters were applied, including DC Bias removal, Butterworth bandpass filter, background removal, and SEC gain. An automated FATT selection routine (figure 6-1) was used for the first pass. Then each selection was manually checked and corrected as needed. Some traces were too distorted to easily distinguish the onset of a signal. They were removed from the dataset.

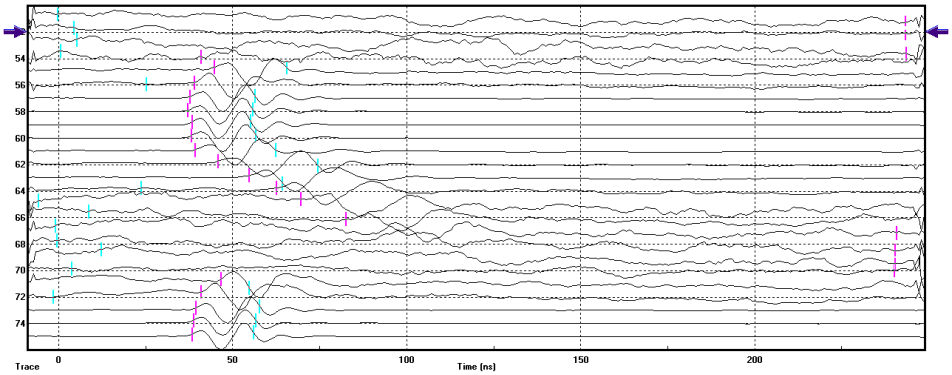

Figure 6-1, An example of the First Arrival Travel Time automatic selection interface. FATTs are indicated by purple marks.

These data were then loaded into ReflexW (Sandmeier Geophysical Research) and repositioned to correct for the true transmitter and receiver locations. Gaussian raytracing was applied at a 0.1 meter resolution and the model in inverted using LSQR with a maximum iterations of 1,000 per inversion. The maximum number of tomography iterations (raytracing then inversion) was 25. The completed tomogram was exported to a comma separated value file and loaded into R (Ihaka, R. and Gentleman, R.) for post-processing. Bivariate spline interpolation was performed on the data using the Akima library (Akima, 1996; Gebhardt, 2015). The image was then smoothed using the "fields" library. A kernal density smoother was applied by taking convulation using a Fast-Fourier-Transform and then normalizing the data using a Nadaraya-Watson estimator (Nychka et al., 2015).

6.8 Results

GPR tomography provides a high-resolution two-dimensional image of the sub-surface by measuring electromagnetic properties that are correlated to geological material properties. To model the sub-surface, several assumptions must be made, such as the path of wave propagation through the media. Because of the complexity of error estimation, the engineer must rely on other information to confirm the results of the tomography. A simple method is to plot the Zero-Offset Profile (ZOP) and compare it to the Multiple-Offset Gathering (MOG) results. Since the ZOP is not affected by curved-ray parameters it is a true representation of the cross-section in one-dimension.

The common feature among the four ZOP cross-sections shown in Figure 6-2 is the radar velocity through the limestone formation below the water table (6 meters below ground surface). The profile shows an approximately vertical line of consistent limestone of roughly 30% porosity. In ZOP A to B, radar velocity increases above the water table, as expected from a decrease in moisture content, to a radar velocity for limestone of nearly 80%. This is beyond the practical limits for porosity. A void, or sand filled cavity, is expected along this horizon. ZOP B to C shows a similar trend. However useful data could not be obtained in this region, possibly due to ground-to-air waves. The ZOP C to D shows little change in the

clay layer above the water table. A possible reflection of the low hydraulic conductivity of clay. The final profile, ZOP D to A, shows a sharp increase in radar velocity. This may be due to the low matric suction potential above the void located in Boring B and inferred in ZOP A to B. Radar velocity then reduces significantly through the clay and rock layer observed in Boring D before increase again near land surface to values approximating loose, dry sand of roughly 40% porosity.

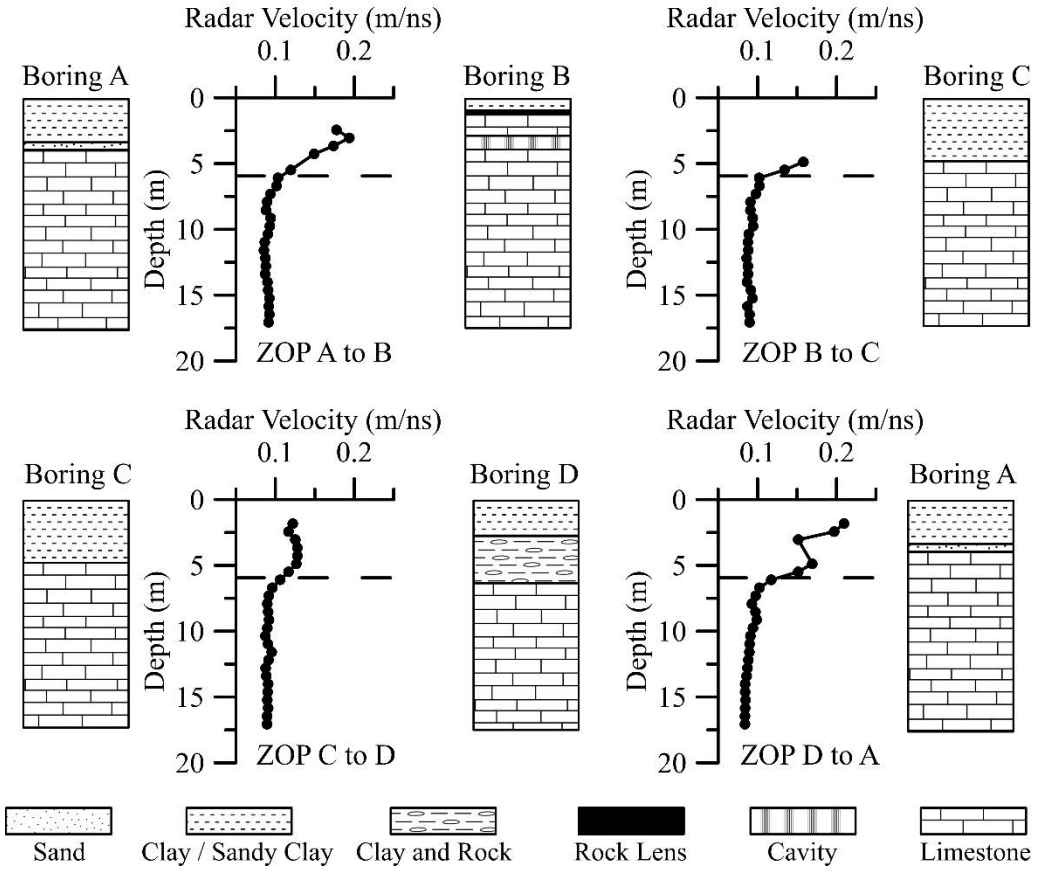

Figure 6-2,Comparison of the Zero-Offset Profile (ZOP) results and the stratigraphy from the driller's logs.

The MOG tomograms (Figure 6-3) follow a similar pattern to the ZOP. In general, there are two distinct zones separated by the water table: a low permittivity upper zone and a high permittivity lower zone. Permittivity changes along the horizontal axis are subtle. The most significant changes are observed

around the void located in Boring B. In MOG A to B, the void is characterized as very low permittivity and extends most of the distance between borings. The void overlays an area of highly weathered limestone, which may have transitioned into sand. This weathered unit may correspond to the thin sand layer observed in Boring A. Starting around roughly 5 meters below ground surface to 8 meters below ground surface, the MOG A to B tomogram expects a weathered limestone unit that overlays a relatively competent limestone formation of roughly 30% porosity. The general stratigraphy of these limestone units carries over to MOG B to C. Here the void extends almost halfway between Boring B and Boring C. The underlying weathered unit tapers towards Boring C and has relative permittivity corresponding to clayey materials. The low hydraulic conductivity of clay and the generally small pore sizes provide potential to maintain saturation within proximity of the water table. However, it appears that the void prevents matric suction from forming. A capillary rise is not overserved in this location. These clays transition to MOG C to D in the same relative placement as indicated in Boring C with a higher relative bulk permittivity than found in the previous MOG. Since the clay material are found at or near the water table without discontinuity, it's expected that the water level rises into the layer. The clay layer pinches upwards nearly 4 meters from Boring C and transitions to a clay and rock layer, which is characterized by a lower permittivity. Below the rock layer competent limestone is found at the interface between the layers--slightly closer to land surface than in the adjacent cross-sections. It may be possible that clays form a confining layer that prevents runoff from weathering the limestone units. Continuing into MOG D to A, the relative bulk permittivity corresponding to the rock layer abruptly stops a little more than 1 meter from Boring D. The relative bulk permittivity then transitions to represent a predominantly clay material, as seen in Boring A. Below this clay layer, the weathered limestone resumes. Limestone of an approximately 40% porosity is found slightly above the water table and continues to 8 meters below grade. The interface between limestone units has a slight taper as it transitions to the material found in MOG A to B.

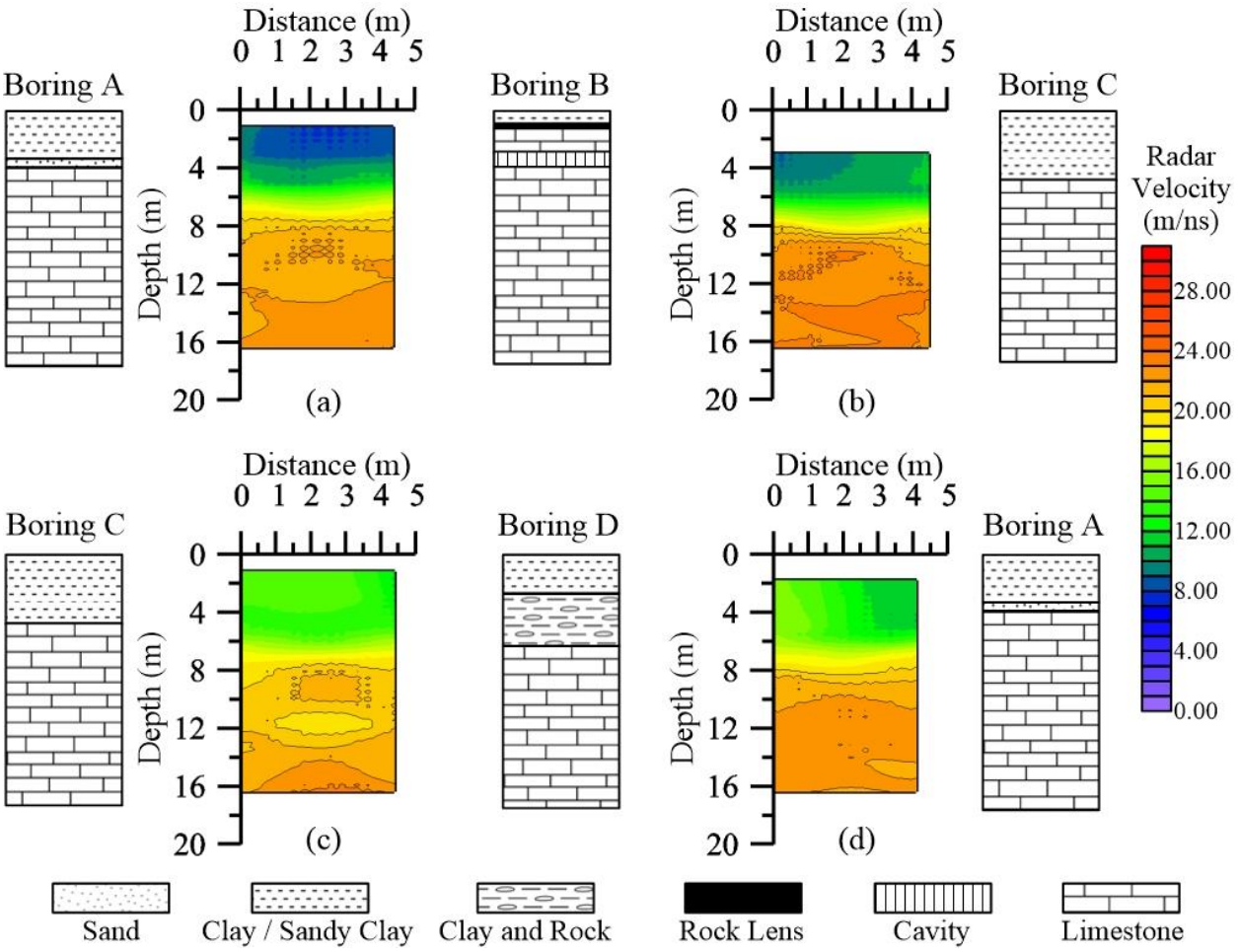

Figure 6-3, Comparison of the Multiple-Offset Gather (MOG) results and the stratigraphy from the driller's log.

6.9 Chapter Summary

In this chapter, tomography is performed on field data collected from a series of boreholes in Newberry, FL. After the data was collected with GPR antenna and data loggers, it was filtered in a computer environment to increase the signal-to-noise ratio. The first arrival travel time was calculated from the improved signal. The data was loaded into ReflexW to develop the tomogram. Gaussian raytracing was used with LSQR inversion. The final tomograms are compared to the driller's logs and expected values from the zero-offset profile. The lithology compares well with the observed data and notable features, such as voids, are identified and occur in formations expected within karst limestone.

Chapter 7
CONCLUSION

In this work, the mathematical basis and practical techniques for Ground Penetrating Radar (GPR) tomography were investigated. GPR tomography is developed from Maxwell's Equations describing electromagnetic responses of the material and from Huygens' Principal describing the propagation of an electromagnetic wavefront. From this foundation, a model is created to better understand how to interpret geological materials from dielectric properties deduced from passing radar waves through a cross-section. Using the Time-Propagation Mixing Model, the geology is decomposed into the geotechnical parameters: lithology, porosity, and saturation. The variation of these parameters is then studied within the geological framework to develop models to describe the spatial variation within the media, such as increasing porosity with depth and matric suction potential above the water table. By passing penetrating GPR waves through the material and measuring the response, these complex geometries can be observed in situ.

This study was comprised of five components. The first component described the physical phenomenon of electromagnetic waves, antenna construction, and wave attenuation. Within this section the electromagnetic properties of geological materials are discussed with insight into methods to reduce the signal variation into physical properties of natural media. This method was developed by Roth (1990) based on the volumetric fraction of two distinct permittivities: water and air. It represents an improvement over the site-specific porosity models developed by Topp et al. (1980).

The second component described how the GPR wave travels throughout and interacts within the material. The full waveform can be simplified into two major families of solutions: raytracing solutions,

which define paths parallel to the expansion of the full GPR wave, and wavefront solutions, which define a contour perpendicular to the expansion of the full GPR wave. There are two common techniques for ray tracing: Geometric Raytracing and Gaussian Raytracing. Geometric Raytracing steps through the material and reflects or refracts across the interface of different material types. Due to the discretization of the sub-surface, errors can be introduced from critically refracted rays by incorrectly creating contrasting boundaries from subtle transitions or model errors. Gaussian Raytracing resolves this issue by finding the weighted average along the wavefront perpendicular to the ray. Thus, smoothing the ratio of change between the contrasting boundaries.

Wavefront solutions have two common techniques. Both techniques intend to solve the Eikonal Equations for Maxwell's equation from a propagating wavefront. The two methods are NORSAR wavefront construction and Fast Marching Methods. Norsar wavefront construction builds the leading envelope for the wavefront by assuming secondary point sources along the previous wavefront. The next wavefront is the curve tangent to these point sources. Alternatively, the Fast Marching Method begins at the source location and moves cell-by-cell through the cross-section. Fast Marching Methods are better adapted for complex profiles with significant changes in velocity. A final method is considered where the raytracing and wavefront methodologies are combined, called Huygens' Wavefront Expansion. In this method, the wavefront is drawn from raytracing parameters. Such that a family of rays is extended from the source to discrete contours. These contours form the wavefront.

The third component described the inversion techniques required to transform field data and raytracing into an image representation of the subsurface. In general, tomography represents a large, sparse ill-conditioned matrix with inherit errors. The matrix dimensions, computer memory limitations, and numerical inaccuracies favor the use of iterative methods to solve the system using the pseudo-inverse of a conditioned matrix. The easiest to implement and least efficient method is Ordinary Least Squares, where the L-2 norm is minimized by iterative corrections to an initial assumption of the true

matrix form. This method is refined by determining the magnitude and direction of the next step using Conjugate Gradient methods. This method creates orthogonal search directions and finds the minimum residual using the surface gradient. While effective, it's is best suited for linear, positive-definitive matrices. These methods can be thought of as development tools for the efficient LSQR; a Least Squares method to solve the QR factorization from orthogonal matrices. The LSQR method is a considerably more complex implementation that is expected to solve the system with less iterations and less computational work. Its stability in solving severally ill-conditioned large sparse matrices makes it the most common inversion technique for commercial software packages.

The fourth component described how the previous sections are used to develop an ideal model to compare the benefits and limitations of each method. Three geological cross-sections were defined, each focusing on a different geotechnical parameter of the T-P Mixing Model and increasing in spatial complexity. The first model simply describes the permittivity values of a homogenous lithology with simple layering. The second model adds depth varying porosity to the model and an air-filled void to induce critical refraction of the radar waves. The final model adds saturation in addition to the other parameters. Since water has a permittivity value almost an order of magnitude higher than other geological media, saturation can have a significant effect on GPR wave propagation. These parameters are included on a model with several lithologies, a dipping bedding plane, and a partially water filled void. Each of the raytracing methods are compared for each of the three geological models. The greatest difference between the methods is observed in the most complex cross-section. Next, a comparison on the inversion techniques is performed for each of the profiles. The methods are similar across all three models. LSQR performs the most favorably in each, yet because Conjugate Gradient requires less computation work per iteration is it comparable to the other methods even though more iterations are required. For simple geometries, there is little benefit to using LSQR over Ordinary Least Squares, for example, but as more complex media is considered the benefits of LSQR become apparent.

The final component of this study collected field data and used the previous methodologies to develop a tomogram of an unknown in situ geological cross-section. The data was collected from four boreholes using Multiple Offset Gathering (MOG) techniques. The information was then filtered and processed to find the first arrival travel time for each trace. Using the antenna locations and the travel times, the dielectric properties of the unknown material between the antenna was determined through raytracing and inversion. The dielectric properties where then related to geotechnical properties that were used to classify and describe the material. This information was compared to Zero-Offset Profile (ZOP) data, which is not expected to have errors inherit in raytracing, and lithology reports in the driller's logs.

7.1 Future Work

GPR tomography is a diverse field ranging across several engineering disciples. This study explored only a small portion of the current research. In addition to first arrival travel time tomography, as described in this work, the full waveform can be incorporated into the tomographic model using finite-difference time-domain inversion techniques (Ernst et al. 2007). Another common variation is to develop the tomogram using the attenuated signal from the material to supplement dielectric properties (Giroux, 2007). Liu et al (1998) have developed formulations to reliably measure attenuation using a predictable shift in the frequency-domain of the received signal. This technique can also be used to correct attenuation effects in conventional travel time tomography (Neto, 2006). Uncertainty in raytracing and inversion techniques can be defined using cokriging of the parameter matrix through geostatistical inversion (Gloaguen, 2005), Markov chain Monte Carlo methods (Seok-Hoon and Byung-Doo, 2001), or Entropy-Bayesian inversion (Hou et al., 2013).

REFERENCES

Akima, H. (1996). Algorithm 760: Rectangular-grid-data surface fitting that has the accuracy of a bicubic polynomial. *ACM Transactions on Mathematical Software 22(3)*, 362-371.

Aldridge, D., & Oldenburg, D. (1993). Two-dimensional tomographic inversion with finite-difference travel times. *J. Seismic Exploration 2*, 257-274.

Alkhalifah, T., & Fomel, S. (2001). Implementing the fast marching eikonal solver: spherical versus cartesian coordinates. *Geophysical Prospecting 49*, 165-178.

Annan, A. (1996). *Ground Penetrating Radar: Workshop.* Misissauga, Ontario: Sensors and Software, Inc.

Annan, A. (2009). Electromagnetic principles of ground penetrating radar. In H. Jol, *Ground Penetrating Radar: Theory and Applications* (pp. 1-37). New York: Elsevier.

Audebert, F., Devc, B., Biondi, B., Lumley, D., Nichols, D., Palacharia, G., . . . Urdaneta, H. (2001). Review of Traveltime computational Methods. *Stanford Exploration Project, Report 80*, 1-48.

Bellefleur, G., Chouteau, M., & Senechal, P. (2000). Potential pitfalls for amplitude inversion revealed by overlapping radar surveys. *Proc of GPR'2000*, (pp. 126-131). Gold Coast, Austrailia.

Bjorck, A., & Elfving, T. (1978). Accelerated projection methods for computing pseudoinverse solutions of systems of linear equations. Linkoping, Sweden: Dept. Math. Linkoping Univ.

Brooks, H. (1967). Rate of solution of limestone in the karst terrain of Florida. *Florida Water Resources Research Center, Univ of Florida, Pub. No. 6*.

Campbell, K., & Scott, T. (1991). Radon potential study, Alachua County, Florida: Near-surface straitigraphy and results of drilling. *Fl Geol. Survey, Open File Report 41, EPA 68D00097*.

Cassiani, G., & Binley, A. (2005). Modeling unsaturated flow in a layered formation under quasi-steady state conditions using geophysical data constraints. *Advances in Water Resources, 28(5)*, 467-477.

Cassidy, N. (2009). Electrical and magnetic properties of rocks, soils, and fluids. In H. Jol, *Ground Penetrating Radar: Theory and Applications, 2e* (pp. 41-67). New York: Elsevier.

Cerveny, V. (1987). Raytracing algorithms in three-dimensional laterally varying layer structures. *Seismic tomography*, 99-133.

Cerveny, V. (2001). *Seismic Ray Theory.* Cambridge University Press.

Cerveny, V., Iversen, E., & Psencik, I. (2012). Two-point Paraxial Traveltimes in an Inhomogeneous Anisotrpoic Medium. *Geophys. J. Int. 189*, 1597-1610.

Chacon, A., & Vladimirsky, A. (2011). Fast two-scale methods for eikonal equations. *Cornell University Department of Mathematics.* National Science Foundation.

Chander, R. (1975). On tracing seismic rays with specified end points. *J. Geophysics 41*, 173-177.

Comas, X., Slater, L., & Reeve, A. (2005). Spatial variability in biogenic gas accumulations in peat soils is revealed by ground penetrating radar (GPR). *Geophysical Research Letters 32(8)*.

Corin, T., Couchard, I., Dethy, B., Haleux, L., Montjoie, A., Richter, T., & Wauters, J. (1997). Radar tomography applied to foundation in a karstic environment. *Modern geophysics in engineering geology*.

Daniels, D. (2007). *Ground Penetrating Radar, 2e.* UK: Institution of Engineering and Technology.

Day-Lewis, F., Lane, J., Harris, J., & Gorelick, S. (2003). Time-lapse imaging of saline-tracer transport in fractured rock using difference-attenuation radar tomography. *Water Resources Research 39(10)*.

Dines, K., & Lytle, R. (1979). Computerized geophysical tomography. *Proc. IEEE 67*, 1065-1073.

Engdahl, E. (1973). Relocation of intermediate depth earthquakes in the Central Aleutian by seismic raytracing. *Nature Physical Sciences 425*, 23-25.

Ernst, J., Green, A., Maurer, H., & Holliger, K. (2007). Application of a new 2D time-domain full-waveform inversion scheme to crosshole radar data. *Geophysics 72 (5)*, J53-J64.

Gebhardt, A. (2015). *akima: interpolation of irregularly and regularly spaced data.* Retrieved from https://CRAN.R-project.org/package=AKIMA

Giroux, B., & Gloagen, E. (2011). Geostatistical traveltime tomography in elliptically anisotropic media. *Geophysical prospecting 60*, 1133-1149.

Giroux, B., Gloaguen, E., & Chouteau, M. (2007). bh_tomo: A Matlab borehole georadar 2D tomography package. *Computers and Geosciences 33*, 126-137.

Gloagen, E., Giroux, B., Marcotte, D., & Dimitrakopoulos. (2007). Pseudo-full-waveform inversion of borehole GPR data using stochastic tomography. *Geophysics Vol. 72*, J43-J51.

Gloagen, E., Marcotte, D., Chouteau, M., & Perroud, H. (2005). Borehole radar velocity inversion using cokriging and cosimulation. *J. Applied Geophysics*, 242-259.

Gloaguen, E., Chouteau, M., Marcotte, D., & Chapuis, R. (2001). Estimation of hydraulic conductivity of an unconfined aquifer using cokriging of GPR and hydrostratigraphical data. *JAG 47*, 135-152.

Gluyas, J., & Cade, C. (1997). Prediction of porosity in compacted sands. *AAPG Memoir 69: Reservoir quality prediction in sandstones and carbonates*, 19-27.

Golub, G., & Kahan, W. (1965). Calculating the singular values and pseudoinverse of a matrix. *SIAM J. Numerical Analysis 2*, 205-224.

Gremaud, P., & Kuster, C. (2004). *Computational study of fast methods for the eikonal equation.* Raleigh, NC: North Carolina State University.

Griffiths, D. (1999). *Introduction to Electrodynamics.* Upper Saddle River, N.J.: Prentice Hall.

Herman, R. (2001). An introduction to electrical resistivity in geophysics. *Am. J. Phys. 69 (9)*, 943-952.

Hestenes, M. (1973). Iterative methods for solving linear equations. *J. Optimization Theory and Applications 11 (4)*, 323-334.

Hou, Z., Terry, N., & Hubbard, S. (2013). *Entropy-Bayesian inversion of time-lapse tomographic GPR data for monitoring dielectric permittivity and soil moisture variations.* Richland, Washington: U.S. Department of Energy.

Hyndman, D., & Tronicke, J. (2005). Hydrogeophysical case studies at the local scale: the saturated zone. In Y. Rubin, & S. Hubbard, *Hydrogeophysics* (pp. 391-412). Netherlands: Springer.

Irving, J., Knoll, M., & Knight, R. (2007). Improving crosshole radar velocity tomograms: A new approach to incorporating high-angle traveltime data. *Geophy. 72(4)*, 31-41.

Jones, G., Upchurch, S., & Champion, K. (1994). *Origin of nitrate in ground water discharging from Rainbow Springs, Marion County, Florida.* Southwest Florida Water Management District Ambient Ground-Water Quality Monitoring Program Report.

Julian, B., & Gubbins, D. (1977). Three-dimensional seismic ray tracing. *J. Geophysics 42*, 95-113.

Kabanikhan, S. (2008). Definitions and examples of inverse and ill-posed problems. *J. Inv. Ill-posed Problems 16*, 317-357.

Kaufmann, M., & Glassner, A. (2002). *An Introduction to Ray Tracing.* San Francisco, CA: Morgan Kaufmann Publishers, Inc.

Keho, T., & Kelamis, P. (2009). A new era in land seismic: The near-surface challenge. *SEG Expanded Abstract 28*, 3421-3425.

Keller, H. (1968). *Numerical methods for two-point boundary value problems.* Waltham, Mass: Blaisdell.

Knight, R., Tercier, P., & Jol, H. (1997). The role of ground penetrating radar and geostatistics in reservoir description. *Leading Edge Vol 16*, 1576-1581.

Kong, T. (1995). Radar tomography for non-destructive testing. *Proc. Intl. Sym. Non-Destructive Testing in Civil Engineering*, (pp. 681-688). Berlin, Germany.

Lehikoinen, A., Finsterle, S., Voutilainen, A., & Kaipio, J. (1997). Approximation errors and truncation of computational domains with application to geophysical tomography. *Inverse Problems and Imaging 2 (2)*.

Likos, W., Lu, N., & Godt, J. (2013). Hysteresis and uncertainty in soil-water retention curve parameters. *J. Geotech Geoenvironmental Engineering*.

Liu, L., Lane, J., & Quan, Y. (1998). Radar attenuation tomography using the centroid frequency downshift method. *J. Applied Geophysics 40*, 105-116.

Liu, Q., & Gu, Y. (2012). Seismic imaging: From classical to adjoint tomography. *Tectonophysics 556-557*, 31-66.

Loke, M. (2004). Tutorial : 2-D and 3-D electrical imaging surveys. *University of Alberta*.

Lomax, A. (1994). The wavelength-smoothing method for approximating broad-band wave propagation through complicated velocity structures. *Geophysical Journal International 117*, 313-334.

Longino, B., & Kueper, B. (1999). Non-wetting phase retention and mobilization in rock fractures. *Water Resources Research 35(7)*, 2085-2093.

Lytle, R., Dines, K., Laine, E., & Lager, D. (1978). *Electromagnetic Cross-Borehole survey of a site proposed for an urban transit station.* Lawrence Livermore Laboratory, Univ. of California.

Malladi, R., Sethian, J., & Vemuri, B. (1996). A fast level set based algorithm for topology-independent shape modeling. *J. Math. Imaging and Vision 6 (2/3)*, 269-290.

Manger, G. (1963). Porosity and bulk density of sedimentary rocks. *USGS 1144-E*.

Marella, R., & Berndt, M. (2005). Water Withdrawals and Trends from the Floridan Aquifer System in the Southeastern United States, 1950-2000. *USGS Circular 1278*.

Meyer, P., Rockhold, M., & Gee, G. (1997). Uncertainty analyses of infiltration and subsurface flow and transport for SDMP sites. *U.S. Nuclear Regulatroy Commission*.

Neto, P. (2005). A practical approach to correct attenuation effects in GPR data. *J. Applied Geophysics*, 140-151.

Nordmann, A. (2007). Refraction in the manner of Huygens.

Nowack, R. (1992). Wavefronts and solutions of the Eikonal Equation. *Geophys. J. Int. 110*, 55-62.

Nychka, D., Furrer, R., Paige, J., & Sain, S. (2015). *fields: Tools for Spatial Data.* Retrieved from https://CRAN.R-project.org/package=fields

Oh, S.-H., & Kwon, B.-D. (2001). Geostatistical approach to bayesian inversion of geophysical data: Markov chain Monte Carlo method. *Earth Planets Space 53*, 777-791.

Olhoeft, G. (1998). Electrical, magnetic, and geometric properties that determine ground penetrating radar performance. *Proc. 7th International Conference on Ground Penetrating Radar* (pp. 477-483). Univ of Kansas: Radar Systems and Remote Sensing Laboratory.

Paige, C., & Saunders, M. (1982). LSQR: An algorithm for sparse linear equations and sparse least squares. *ACM Transactions on mathematical software 8 (1)*, 43-71.

Pujol, J. (2007). The Solution of Nonlinear Inverse Problems and the Levenburg-Marquardt Method. *Geophys. SEG 72 (4)*, 1-16.

Rao, S. (2002). *Applied Numerical Methods for Engineering and Scientists.* Prentice Hall.

Roberts, S., & Shipman, J. (1972). *Two-point boundary value problems.* New York: Elsevier.

Roth, K., Schulin, R., Fluhler, H., & Attinger, W. (1990). Calibration of time domain reflectometry for water content measurement using a composite dielectric approach. *Water Resources Research 26*, 2267-2273.

Sava, P., & Fomel, S. (1997). Huygens wavefront tracing: a robust alternative to conventional ray tracing. *SEP Report 95*, 101-113.

Scott, T. (2001). Text to accompany the geological map of Florida. *Fl. Geol. Survey, Open File Report 80*.

Sethian, J. (1998). Fast marching methods and level set methods for propagating interfaces. *Computational Fluid Mechanics.* von Karman Institute Lecture Series.

Shewchuk, J. (1994). *An Introduction to the Conjugate Gradient Method.* Pittsburgh, PA: Carnegie Mellon University, School of Computer Science.

Stewart, J. (1982). Ground-water degradation incidents, west-central Florida, in Environmentally Sound Water and Soil Management. *Irrigation and Drainage Division* (pp. 445-452). Orlando, Florida: American Society of Civil Engineers.

Strang, G. (2007). *Computational Science and Engineering.* Wellesley-Cambridge Press.

Topp, G., Davis, J., & Annan, A. (1980). Electromagnetic determination of soil water content-measurement in coaxial transmission lines. *Water Resources Research 16*, 574-582.

Truss, S., Grasmueck, M., Vega, S., & Viggiano, D. (2007). Imaging rainfall drainage within the Miami oolitic limestone using high-resolution time-lapse ground-penetrating radar. *Water Resources Research 43(3)*.

Tsoflias, G., Van Gestel, J., Stoffa, P., Blankenship, D., & M., S. (2004). Vertical fracture detection by exploiting the polarization properties of ground-penetrating radar signals. *Geophysics 69(3)*, 803-810.

Tweeton, D. (2008). Wavefront Construction. In *GeoTom CG* (pp. 60-70).

Urdaneta, H. (1994). Wavefront construction using waverays. *SEP Report 80*, 85-100.

van Genuchten, M. (1980). A closed-form equation for predicting hydraulic conductivity of unstaturated soils. *Soil science society of America journal*, 892-898.

Veselov, A. (2002). Huygens' Principle. Loughborough University.

Vinje, V., Inverson, E., & Gjoystdal, H. (1993). Traveltime and amplitude estimation using wavefront construction. *Geophysics 58*, 1157-1166.

Wesson, R. (1971). Travel time inversion for laterally inhomogenous crustal velocity models. *Bulletin of the Seismic Society of America*, 729-746.

Wolf, K. (1995). Geometry and dynamics in refracting systems. *EU J. Phy. 16*, 14-20.

Yilmaz, O., & Doherty, S. (1987). Seismic Data Processing: Investigations in Geophysics. Tulsa, Oklahoma: Society of Exploration Geophysics.

Zhang, L. (1993). Imaging by the wavefront propagation method. *Ph.D thesis*. Stanford Univ.

Zhdanov, M. (1993). *Regularization in Inversion Theory.* Golden, CO: Center for Wave Phenomena, Colorado School of Mines.

Vita

The author, D. Craig Jones, graduated with a Bachelor of Science in Civil Engineering from the University of North Florida in May, 2010 specializing in water resources with elective coursework in spatial systems and numerical modeling. Afterwards, he worked as the Operations Engineer for JEA overseeing the 135 water production wells in the service area with capacities ranging from 500 gallons per minute to 4,000 gallons per minute. Currently, Craig is a professional engineer in the water and wastewater system planning division focusing on hydraulic modeling. The system consists of roughly 3,000 pumps; 4,000 miles of forcemain and gravity pipelines; and 5,000 miles of pressurized potable water and reclaimed water distribution piping. He is familiar with several programming languages and enjoys work in data analytics. His free time is spent with family and travelling, especially to Montana and the surrounding areas.

Publications

Jones, D.C., & Hudyma, N. (2016). Characterization of Weather Limestone Using Cross-Hole Ground Penetrating Radar Techniques. *Geo-Chicago.* Chicago, IL.

Jones, D.C., & Hudyma, N. (2016). The influence of ray density on the GPR cross borehole tomographic inversion of a synthetic limestone formation with karst features. *Florida Academy of Sciences.* St. Petersburg, FL.